International Journal of Optics

Optical Techniques for Measuring Object Shape and Appearance

Lead Guest Editor: Changsoo Je
Guest Editors: Zhenzhou Wang, Xintao Ding, Hao-Chiang Shao, and Chi Zhang

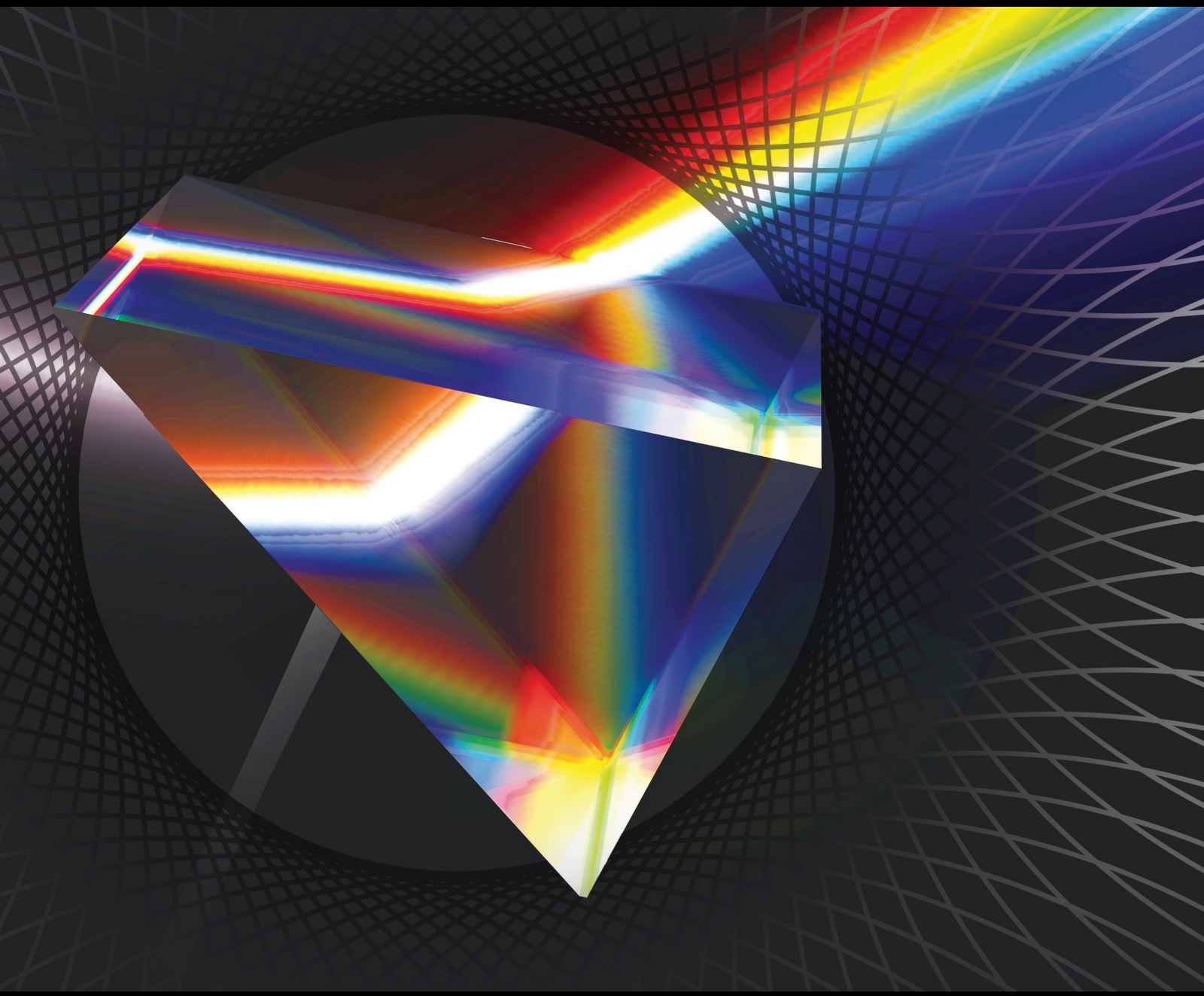

Optical Techniques for Measuring Object Shape and Appearance

International Journal of Optics

Optical Techniques for Measuring Object Shape and Appearance

Lead Guest Editor: Changsoo Je
Guest Editors: Zhenzhou Wang, Xintao Ding, Hao-Chiang Shao, and Chi Zhang

Chief Editor

Academic Editors

Contents

A Unified Shape-From-Shading Approach for 3D Surface Reconstruction Using Fast Eikonal Solvers
Guohui Wang, Xuan Zhang, and Jin Cheng
Research Article (12 pages), Article ID 6156058, Volume 2020 (2020)

Three-Dimensional Reconstruction of Mechanical Parts Based on Digital Holography
Yaohui Dai, Haiyu Wu, Gang Zhu, and Yan Yang
Research Article (13 pages), Article ID 6712781, Volume 2020 (2020)

Hindawi
International Journal of Optics
Volume 2020, Article ID 6156058, 12 pages
https://doi.org/10.1155/2020/6156058

Research Article

A Unified Shape-From-Shading Approach for 3D Surface Reconstruction Using Fast Eikonal Solvers

Guohui Wang,[1,2] **Xuan Zhang**,[1] **and Jin Cheng**[1]

[1]*School of Opto-Electronic Engineering, Xi'an Technological University, Xi'an 710021, China*
[2]*Shaanxi Province Key Laboratory of Photoelectricity Measurement and Instrument Technology, Xi'an Technological University, Xi'an 710021, China*

Correspondence should be addressed to Guohui Wang; booler@126.com

Received 8 November 2019; Revised 10 March 2020; Accepted 8 May 2020; Published 29 May 2020

Guest Editor: Changsoo Je

Object shape reconstruction from images has been an active topic in computer vision. Shape-from-shading (SFS) is an important approach for inferring 3D surface from a single shading image. In this paper, we present a unified SFS approach for surfaces of various reflectance properties using fast eikonal solvers. The whole approach consists of three main components: a unified SFS model, a unified eikonal-type partial differential image irradiance (PDII) equation, and fast eikonal solvers for the PDII equation. The first component is designed to address different reflectance properties including diffuse, specular, and hybrid reflections in the imaging process of the camera. The second component is meant to derive the PDII equation under an orthographic camera projection and a single distant point light source whose direction is the same as the camera. Finally, the last component is targeted at solving the resultant PDII equation by using fast eikonal solvers. It comprises two Godunov-based schemes with fast sweeping method that can handle the eikonal-type PDII equation. Experiments on several synthetic and real images demonstrate that each type of the surfaces can be effectively reconstructed with more accurate results and less CPU running time.

1. Introduction

In the field of computer vision, object shape reconstruction from images has been an active topic. There are several techniques, such as stereo vision, structured light, fringe projection profilometry, and shape-from-X (X = shading, photometric stereo, texture, focus/defocus, motion, etc.). Shape-from-shading (SFS) is an important approach for inferring 3D surface from a single shading image and because of its simplicity of equipment, it is widely used in face reconstruction [1, 2], 3D reconstruction of medical images [3, 4], lunar surface reconstruction [5, 6], and so on. It was initiated by Horn [5] who firstly formulated a first-order partial differential image irradiance (PDII) equation describing the relations between the 3D shape of a surface and its corresponding 2D variation of intensities. Thus one can determine 3D surface by starting with the PDII equation.

Since Horn's original work, a great number of different SFS approaches have come out (for surveys, refer to Zhang et al. [7], and Durou et al. [8]). There are mainly two steps when utilizing an SFS approach. The first step is meant to model the image formation process of the camera which is determined by the reflectance property of the surface, the light source, and the camera projection and to derive the PDII equation under certain assumption [9]. The second step is targeted at designing a numerical scheme to solve the resultant PDII equation. Most of the SFS approaches concentrate on how to design an effective numerical scheme assuming that the surface obeys a simple Lambertian reflection. These approaches are generally divided into two classes: partial differential equation- (PDE-) based methods and optimisation methods [10, 11]. The characteristics-based approach [5] and the viscosity solution-based approaches [1, 3, 4, 9–16] can be categorized into the first class. We should mention the pioneering viscosity solution-based approach of Rouy and Tourin [12], who first described the PDII equation under Lambertian reflectance model as a Hamilton-Jacobi-Bellman PDE and got a nonclassical

solution based on viscosity solution theory. Kimmel and Sethian [13] transformed the PDII equation under the vertical light into an eikonal-type PDE and used the first-order fast marching method [17] to solve its viscosity solution. For the oblique light case, Governi et al. [14] reconstructed the initial surface by directly using the fast marching method [17]. They rotated the normal map obtained from the surface around the oblique light and then computed the "new" image as the dot product between the normal map and vertical light. The final surface could be reconstructed by applying the fast marching method to the "new" image again. The works of [5, 7, 8, 10–14] are thinking of an orthographic projection for the camera. As for perspective camera projection, Prados and Faugeras [1] related the PDII equation to a Hamiltonian based on the work [12] and got its viscosity solution with optimal control theory. Breuss et al. [15, 16] analytically and numerically studied the perspective PDII equation formulated by Prados and Faugeras [1] and the associated Hamilton-Jacobi PDE. At the same time, they proved the convergence of the finite-difference and the semi-Lagrangian schemes for the resultant PDE. The second class means the minimisation methods for the SFS problem [7]. Ikeuchi and Horn [18] formulated SFS as a minimisation problem of the difference between observed intensities and the expected intensities that are given through the PDII equation from the expected surface normal, on which the smoothness constraint was used. Tankus et al. [19] first derived a perspective PDII equation and obtained an approximate solution under the assumption that the surface is locally paraboloidal. The 3D shape was reconstructed by minimising a quadratic cost functional. More recently, Santo et al. [20] revisited the numerical SFS approach of Ikeuchi and Horn [18] and described corresponding solution that was built upon different convex relaxation strategies. It is worth mentioning that Quéau et al. [21] combined the advantages of optimisation methods and PDE-based methods and built a generic variational solution that is suitable for SFS under natural illumination and can handle a variety of scenarios for various lighting and camera projection.

While most of the SFS approaches assume the Lambertian reflection, there are a few researchers who are interested in non-Lambertian SFS since the Lambertian reflectance model has been proved to be inaccurate, especially for rough diffuse surfaces [22]. Ragheb and Hancock [23] proposed a non-Lambertian SFS with the Oren-Nayar reflectance model and gave two solutions: the lookup table and the analytic solution. Ahmed and Farag [24, 25] presented several non-Lambertian SFS approaches including Ward SFS and Oren-Nayar SFS and approximated the PDII equations by using the Lax-Friedrichs sweeping scheme [26]. Since the actual convergence to the correct solution is very slow in [25], Vogel and Cristiani [27] applied the Upwind scheme to get a more efficient solution with less convergence time. Tozza and Falcone [10, 28] addressed a general framework for several non-Lambertian SFS problems including Oren-Nayar SFS and Phong SFS, solved by a semi-Lagrangian scheme, and obtained convergence results. However, their framework can only handle a special case where the specular reflection parameter n in the Phong reflectance model [29] equals 1; that is, it represents the worst case. By extending the work of Galliani et al. [30], Ju et al. [4] adopted spherical parameterisation of the surface into the Oren-Nayar PDII equations and thus could compute them at any position of the point light source. However, the fast-marching scheme depicted in Cartesian coordinates needs to be converted to spherical coordinates during the process.

In this paper, motivated by the work of Camilli and Tozza [31] and based on our previous work [11], we first present a unified SFS model for surfaces of different reflectance properties including diffuse, specular, and hybrid reflections in the image formation process. Although our work falls in the situation where the camera performs an orthographic projection and the direction of the single distant point light source is the same as the camera, these reflections lead to more complex nonlinear PDII equations. However, all the PDII equations corresponding to the reflections considered here (Oren–Nayar model and unified model) have a similar structure, so we can look for weak solutions to this class in the viscosity solution sense. Another contribution of our work is that we convert the PDII equation into an eikonal-type PDE through solving a high-order equation by using the Newton-Raphson method, after which we try to obtain the viscosity solution of the eikonal-type PDE by using fast eikonal solvers which are composed of the first- and high-order Godunov-based schemes accelerated by the fast sweeping method.

A similar formulation for the SFS problem of the Oren-Nayar model has been reported in our previous work [11]. As we said, in this paper we will focus our attention on the unified reflectance model (including Lambertian model, Oren–Nayar model, and Blinn–Phong model) and formulate the unified high-order PDII equation under the vertical light. Using the Newton-Raphson method for the resultant PDII equation, we will obtain the eikonal-type PDE that can be solved via fast eikonal solvers presented preliminarily in our work [11].

2. A Unified SFS Model in the Imaging Process

In this section, a very brief description for the Lambertian, Oren–Nayar and Blinn–Phong reflectance model is given in order to setup a unified imaging model.

2.1. Lambertian Reflectance Model. Generally, the Lambertian reflectance is a classical assumption in most of the SFS approaches [1, 3, 5, 8, 12–16, 18–21, 30] for approximating the reflectance property of the diffuse surface. In this case, the surface reflected radiance is addressed as [3]

$$L_r = I_0 \frac{\rho_d}{\pi} \cos\theta_i, \tag{1}$$

where I_0 is the intensity of point light source, ρ_d is the diffuse albedo which controls the proportion of incident light that is reflected diffusely, and θ_i is the angle between the surface unit normal $\mathbf{n}$ and the incident light direction $\mathbf{L}$ illustrated in Figure 1.

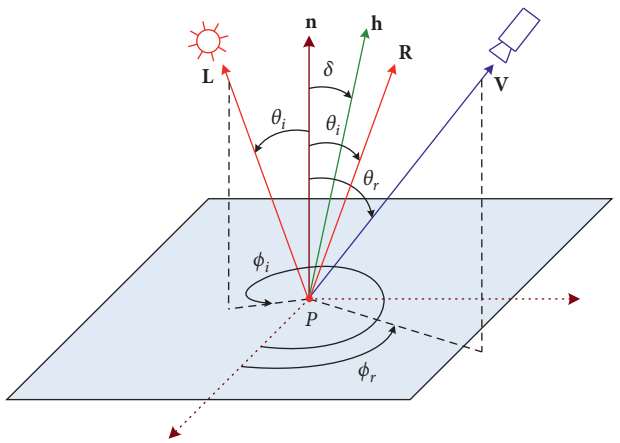

FIGURE 1: Reflection geometry of a local surface point. **n** is the unit normal of the surface point P; (θ_r, ϕ_r) and (θ_i, ϕ_i) are the camera direction **V** and incident light direction **L**, respectively; **R** is reflected light direction; **h** is the unit angular bisector of **V** and **L**; that is, $\mathbf{h} = (\mathbf{V} + \mathbf{L})/\|\mathbf{V} + \mathbf{L}\|$; δ is the angle between **n** and **h**.

2.2. Oren–Nayar Reflectance Model. In order to get rid of the inaccuracy resulting from the assumption of the Lambertian reflectance model for diffuse reflection, Oren and Nayar [22] proposed a comprehensive reflectance model for rough diffuse surfaces.

By assuming that the surface is composed of V-shaped cavities which are symmetric and have two planar facets and that each facet obeys a simple Lambertian reflection, for a Gaussian distribution of the facet normals, they got a simplified expression for the reflected radiance:

$$L_r(\theta_i, \phi_i; \theta_r, \phi_r) = I_0 \frac{\rho_d}{\pi} \cos\theta_i \left(A + B \max[0, \cos(\phi_r - \phi_i)] \sin\alpha \tan\beta\right), \tag{2}$$

where $A = 1 - 0.5\sigma^2/(\sigma^2 + 0.33)$, $B = 0.45\sigma^2/(\sigma^2 + 0.09)$; (θ_i, ϕ_i) is the incident light direction **L**; (θ_r, ϕ_r) is the camera direction **V**; $\alpha = \max[\theta_i, \theta_r]$, $\beta = \min[\theta_i, \theta_r]$. The parameter σ is applied as a measure of the surface roughness, and it denotes the standard deviation of the Gaussian distribution.

For smooth surfaces, we have $\sigma = 0$ and obviously the Oren-Nayar reflectance model degenerate to the Lambertian model in this situation.

2.3. Blinn–Phong Reflectance Model. It is worth mentioning that Phong [29] developed a hybrid reflectance model by introducing a specular component to the surface reflected radiance (1). He described the specular component as a power of the cosine of the angle between the reflected light direction **R** and the camera direction **V**. Hence, the hybrid reflected radiance can be derived in general as

$$L_r = w_d I_0 \frac{\rho_d}{\pi} \cos\theta_i + w_s I_0 \frac{\rho_s}{\pi} \left(\frac{\mathbf{R}}{\|\mathbf{R}\|} \cdot \frac{\mathbf{V}}{\|\mathbf{V}\|}\right)^n, \tag{3}$$

where w_d and w_s are the weighting factors of diffuse and specular components, respectively, and $w_d + w_s \le 1$. ρ_s is the specular albedo that determines the proportion of incident light that is reflected specularly. The parameter n is used to express the specular reflection property of a surface and can be used as a measure of the surface shininess. Obviously, the contribution of the specular component decreases when the value of parameter n increases.

Note that it is not convenient to compute the specular reflected radiance in terms of $(\mathbf{R} \cdot \mathbf{V})$. The Blinn–Phong reflectance model, proposed by Blinn [32], is a modification of the Phong model for computation convenience. Substituting $(\mathbf{n} \cdot \mathbf{h})$ into $(\mathbf{R} \cdot \mathbf{V})$ in formula (3), the hybrid reflected radiance based on the Blinn–Phong model can be formulated as

$$L_r = w_d I_0 \frac{\rho_d}{\pi} \cos\theta_i + w_s I_0 \frac{\rho_s}{\pi} (\mathbf{n} \cdot \mathbf{h})^n. \tag{4}$$

2.4. A Unified Reflectance Model. As mentioned before, the Lambertian reflectance model has been proved to be inaccurate, especially for rough diffuse surfaces. Thus, we can combine diffuse and specular components of a surface through a linear combination of Oren–Nayar model and the specular part of Blinn–Phong model; that is, we substitute surface reflected radiance (2) into the diffuse part of Blinn–Phong model:

$$L_r = w_d I_0 \frac{\rho_d}{\pi} \cos\theta_i \left(A + B \max[0, \cos(\phi_r - \phi_i)] \sin\alpha \tan\beta\right) + w_s I_0 \frac{\rho_s}{\pi} (\mathbf{n} \cdot \mathbf{h})^n. \tag{5}$$

Obviously, surface reflected radiance (5) is a unified reflectance model including the Lambertian, the Oren–Nayar, and the Blinn–Phong model. For $w_s = 0$, it reduces to the Oren–Nayar model. For $\sigma = 0$, it reduces to the Blinn–Phong model. Specially, if $w_s = 0$ and $\sigma = 0$, it degenerates to the Lambertian model.

The following relationship between the surface reflected radiance L_r and the image irradiance E_i of the camera is well known [9]:

$$E_i = L_r \frac{\pi}{4} \left(\frac{D}{f}\right)^2 \cos^4\chi, \tag{6}$$

where D is the entrance pupil diameter of the camera lens whose focal length is f. χ is the angle between the line of sight to an image point of a corresponding surface point and the optical axis of the camera. Even for uniform illumination, the term $\cos^4\chi$ implies nonuniform image irradiance. The actual imaging lens of the camera, however, is generally designed to correct it. Thus, one can consider E_i to be proportional to L_r:

$$E_i = \eta L_r. \tag{7}$$

Substituting equation (5) into (7), and if we set $\rho_d = \rho_s$ to a constant ρ as done in [31] and denote $I = \pi E_i/\eta I_0 \rho$ as done in most of SFS approaches, the image irradiance equation (7) will be rewritten as

$$I = w_d \cos\theta_i \left(A + B\max\left[0,\ \cos\left(\phi_r - \phi_i\right)\right]\sin\alpha\tan\beta\right) + w_s\left(\mathbf{n}\cdot\mathbf{h}\right)^n. \tag{8}$$

3. A Unified Eikonal-Type PDII Equation

In this section, we will formulate the image irradiance equation under the situation where the camera performs an orthographic projection and the direction of the single distant point light source coincides with the camera.

3.1. Nonlinear PDII Equation for the Unified Model. With the basis that the optical axis of the camera is the $z-$axis and the image plane of the camera is the $x - y$ plane, the SFS approach can be described as inferring a 3D surface, $z(x, y)$. Since our work falls in an orthographic camera projection, the first partial derivatives of the surface $z(x, y)$ with respect to x and y, respectively, are

$$\begin{aligned} p(x, y) &= \frac{\partial z(x, y)}{\partial x}, \\ q(x, y) &= \frac{\partial z(x, y)}{\partial y}. \end{aligned} \tag{9}$$

So the unit normal $\mathbf{n}$ at a 3D surface point $P(x, y, z(x, y))$ can be expressed as

$$\mathbf{n}(x, y) = \frac{\left(p(x, y), q(x, y), -1\right)}{\sqrt{1 + p^2(x, y) + q^2(x, y)}} = \frac{(p, q, -1)}{\sqrt{1 + \|\nabla z(x, y)\|^2}}. \tag{10}$$

Considering that the direction of the distant point light source $\mathbf{L}$ is the same as the camera direction $\mathbf{V}$ illustrated in Figure 1, we have $\theta_i = \theta_r$, $\phi_i = \phi_r$, $\alpha = \theta_i = \beta$, and $\mathbf{h} = \mathbf{L}/\|\mathbf{L}\|$, $\mathbf{n}\cdot\mathbf{h} = \cos\theta_i$. Consequently, image irradiance equation (8) will be reduced to

$$I(x, y) = w_d\left(A\cos\theta_i + B\sin^2\theta_i\right) + w_s\cos^n\theta_i. \tag{11}$$

Defining that the direction vectors of $\mathbf{L}$ and $\mathbf{V}$ both are $[0, 0, -1]$; that is, they are parallel to the optical axis of the camera lens, and because θ_i is the angle between $\mathbf{n}$ and $\mathbf{L}$, we have

$$\begin{aligned} \cos\theta_i &= \mathbf{n}\cdot\frac{\mathbf{L}}{\|\mathbf{L}\|} = \frac{1}{\sqrt{1 + \|\nabla z(x, y)\|^2}}, \\ \sin^2\theta_i &= 1 - \cos^2\theta_i = \frac{\|\nabla z(x, y)\|^2}{1 + \|\nabla z(x, y)\|^2}. \end{aligned} \tag{12}$$

Substituting equation (12) into (11), the image irradiance equation (11) can be rewritten as

$$\begin{aligned} I(x, y) = w_d &\left(\frac{A}{\sqrt{1 + \|\nabla z(x, y)\|^2}} + \frac{B\|\nabla z(x, y)\|^2}{1 + \|\nabla z(x, y)\|^2}\right) \\ &+ w_s\left(\frac{1}{\sqrt{1 + \|\nabla z(x, y)\|^2}}\right)^n. \end{aligned} \tag{13}$$

Obviously, the image irradiance equation (13) is a more complex nonlinear PDE and is difficult to solve $z(x, y)$. Applying the change of variable $T = 1/\sqrt{1 + \|\nabla z(x, y)\|^2}$, the PDII equation (13) can be considered as calculating a zero of the function $F(T)$, given by

$$F(T) = w_s T^n - Bw_d T^2 + Aw_d T + Bw_d - I; \quad 0 < T \le 1. \tag{14}$$

3.2. Eikonal-Type PDE for the Oren–Nayar Model. Especially, for $w_s = 0$, that is, for the PDII equation of the Oren–Nayar model, $F(T) = 0$ will lead to a quadratic equation:

$$Bw_d T^2 - Aw_d T + I - Bw_d = 0. \tag{15}$$

Calculating equation (15) and satisfying $0 < T \le 1$, we can obtain

$$T = \frac{Aw_d - \sqrt{\left(Aw_d\right)^2 - 4Bw_d\left(I - Bw_d\right)}}{2Bw_d}. \tag{16}$$

Hence, SFS problem (13) can be rewritten as an eikonal-type PDE:

$$\begin{cases} \|\nabla z(x, y)\| = \sqrt{\dfrac{1}{T^2} - 1}, & \forall (x, y) \in \Omega, \\ \\ z(x, y) = \Gamma(x, y), & \forall (x, y) \in \partial\Omega, \end{cases} \tag{17}$$

where Ω is a given image domain and $\Gamma(x, y)$ is a boundary condition. Similar work has been studied in our previous work [11] and here will be extended to the unified model.

3.3. Eikonal-Type PDE for the Unified Model. For $w_s \neq 0$, $F(T)$ is a high-order function of T when $n > 1$ and it is difficult to calculate the zero values. We can use the Newton–Raphson method to solve it. The derivative of the function $F(T)$ is

$$F'(T) = nw_s T^{n-1} + w_d(A - 2BT) \geq nw_s T^{n-1} + w_d(A - 2B). \tag{18}$$

If the surface roughness $0 \leq \sigma \leq 0.6220$, then $A \geq 2B \geq 0$. At the same time, $0 < T \leq 1$, so $F\prime(T) > 0$ and function $F(T)$ is monotonous. Simultaneously, we have

$$\begin{cases} F(0) = -w_s T^n - w_d T(A - BT) < -w_s T^n - w_d T(A - 2B) < 0, \\ F(1) = w_s(1 - T^n) + w_d(1 - T)(A - B - BT) \geq w_s(1 - T^n) + w_d(1 - T)(A - 2B) \geq 0. \end{cases} \tag{19}$$

Hence, function (14) always has a unique zero. Starting with the value $T^0 = 0$, the iterative equation of the Newton-Raphson method is applied to calculate a new value for T^k as follows:

$$T^k = T^{k-1} - \frac{F(T^{k-1})}{F'(T^{k-1})}. \tag{20}$$

After several numbers of iterations, an accurate zero of function (14) is obtained. Similar to the structure of the Oren–Nayar model, we can get an eikonal-type PDE for the unified model:

$$\begin{cases} \|\nabla z(x, y)\| = \sqrt{\dfrac{1}{(T^k)^2} - 1}, & \forall (x, y) \in \Omega, \\ z(x, y) = \Gamma(x, y), & \forall (x, y) \in \partial\Omega. \end{cases} \tag{21}$$

4. Fast Eikonal Solvers for the Eikonal-Type PDE

In this section, we will use the fast eikonal solvers which are composed of the first-order Godunov-based scheme [12, 33] and high-order Godunov-based scheme [11, 34] accelerated by the fast sweeping method [33, 35] to look for the weak solutions of the resultant eikonal-type PDE (21) in the viscosity solution sense.

4.1. First-Order Godunov-Based Scheme. We use $(x_i, y_j) = (i \times w, j \times w)$ to denote a grid point in the image domain Ω, w to denote the grid size, $M \times N$ to denote the image size, and $z_{i,j} = z(x_i, y_j)$ to denote the numerical solution at the 3D surface $z(x, y)$. The first-order Godunov-based scheme [12, 33] can be employed to discretize resultant eikonal-type PDE (21):

$$\left[\left(\frac{z_{i,j} - z_{i\min}}{w}\right)^+\right]^2 + \left[\left(\frac{z_{i,j} - z_{j\min}}{w}\right)^+\right]^2 = G_{i,j}^2, \tag{22}$$

where $z_{i\min} = \min[z_{i+1,j}, z_{i-1,j}]$, $z_{j\min} = \min[z_{i,j+1}, z_{i,j-1}]$, $G_{i,j} = \sqrt{(1/(T_{i,j}^k)^2) - 1}$, and

$$(x)^+ = \begin{cases} 0, & x < 0, \\ x, & x \geq 0. \end{cases} \tag{23}$$

Thus, the viscosity solution of eikonal-type PDE (21) can be obtained using the first-order Godunov-based scheme:

$$z_{i,j} = \begin{cases} \min\left[z_{i\min}, z_{j\min}\right] + wG_{i,j}, & \left|z_{i\min} - z_{j\min}\right| \geq wG_{i,j}, \\ \dfrac{z_{i\min} + z_{j\min} + \sqrt{2w^2 G_{i,j}^2 - \left(z_{i\min} - z_{j\min}\right)^2}}{2}, & \left|z_{i\min} - z_{j\min}\right| < wG_{i,j}. \end{cases} \tag{24}$$

4.2. High-Order Godunov-Based Scheme. In order to obtain a higher-order accuracy viscosity solution, the high-order Godunov-based scheme [34] can be employed to discretize resultant eikonal-type PDE (21):

$$\left[\left(\frac{z_{i,j}^{\text{new}} - z_{i\min}^{\text{high}}}{w}\right)^+\right]^2 + \left[\left(\frac{z_{i,j}^{\text{new}} - z_{j\min}^{\text{high}}}{w}\right)^+\right]^2 = G_{i,j}^2, \tag{25}$$

with

$$\begin{aligned} z_{i\min}^{\text{high}} &= \min\left[\left(z_{i,j}^{\text{old}} + wp_{i,j}^+\right), \left(z_{i,j}^{\text{old}} - wp_{i,j}^-\right)\right], \\ z_{j\min}^{\text{high}} &= \min\left[\left(z_{i,j}^{\text{old}} + wq_{i,j}^+\right), \left(z_{i,j}^{\text{old}} - wq_{i,j}^-\right)\right], \end{aligned} \tag{26}$$

where $p_{i,j}$ and $q_{i,j}$ need to be approximated with higher-order accuracy. According to [34], third-order weighted essentially nonoscillatory scheme [36] is able to be chosen as $p_{i,j}$ and $q_{i,j}$ approximations:

$$\begin{aligned} p_{i,j}^+ &= (1 - u_+)\left(\frac{z_{i+1,j} - z_{i-1,j}}{2w}\right) + u_+\left(\frac{-z_{i+2,j} + 4z_{i+1,j} - 3z_{i,j}}{2w}\right), \\ p_{i,j}^- &= (1 - u_-)\left(\frac{z_{i+1,j} - z_{i-1,j}}{2w}\right) + u_-\left(\frac{3z_{i,j} - 4z_{i-1,j} + z_{i-2,j}}{2w}\right), \end{aligned} \tag{27}$$

with

$$
\begin{aligned}
u_+ &= \frac{1}{1+2v_+^2},\\
v_+ &= \frac{\varepsilon + \left(z_{i+2,j} - 2z_{i+1,j} + z_{i,j}\right)^2}{\varepsilon + \left(z_{i+1,j} - 2z_{i,j} + z_{i-1,j}\right)^2},\\
u_- &= \frac{1}{1+2v_-^2},\\
v_- &= \frac{\varepsilon + \left(z_{i,j} - 2z_{i-1,j} + z_{i-2,j}\right)^2}{\varepsilon + \left(z_{i+1,j} - 2V_{i,j} + z_{i-1,j}\right)^2},
\end{aligned}
\tag{28}
$$

where ε is a very small number that keeps the denominator from getting too close to zero. Similarly, $q_{i,j}^+$ and $q_{i,j}^-$ can be defined. Now the viscosity solution of eikonal-type PDE (21) can be obtained using the high-order Godunov-based scheme:

$$
z_{i,j}^{\text{new}} = \begin{cases} \min\left[z_{i\min}^{\text{high}}, z_{j\min}^{\text{high}}\right] + wG_{i,j}, & \left|z_{i\min}^{\text{high}} - z_{j\min}^{\text{high}}\right| \geq wG_{i,j}, \\ \dfrac{z_{i\min}^{\text{high}} + z_{j\min}^{\text{high}} + \sqrt{2w^2G_{i,j}^2 - \left(z_{i\min}^{\text{high}} - z_{j\min}^{\text{high}}\right)^2}}{2}, & \left|z_{i\min}^{\text{high}} - z_{j\min}^{\text{high}}\right| < wG_{i,j}. \end{cases}
\tag{29}
$$

4.3. Fast Sweeping Method for Godunov-Based Schemes. In order to speed up the convergence numerical schemes, we take the philosophy of fast sweeping method [33, 35] to the first-order or high-order Godunov-based schemes in the following. When the derivatives $p_{i,j}^+$, $q_{i,j}^+$ and $p_{i,j}^-$, $q_{i,j}^-$ are calculated, the newest available values for z are employed. Meanwhile, the iterations do not sweep in only one direction but in four alternating directions repeatedly: (1) from upper left to lower right, that is, $i = 1{:}\ I$, $j = 1{:}J$; (2) from lower left to upper right, that is, $i = I{:}\ 1$, $j = 1{:}\ J$; (3) from lower right to upper left, that is, $i = I{:}\ 1$, $j = J{:}\ 1$; (4) from upper right to lower left, that is, $i = 1{:}\ I$, $j = J{:}\ 1$. As can be easily seen, various values $z_{i\pm1,j}$, $z_{i\pm2,j}$ and $z_{i,j\pm1}$, $z_{i,j\pm2}$ are to be taken according to the current sweeping direction.

We summarize the fast eikonal solvers for the resultant eikonal-type PDE (21) as follows:

Step 1 (Initialization): according to the boundary condition $z(x, y) = \Gamma(x, y)$, $(x, y) \in \partial\Omega$, assign exact values at the grid points on the boundary $\partial\Omega$, whose values are fixed during iterations. At all other grid points, for first-order Godunov-based scheme, big positive values are used as the initial guess, which are larger than the maximum of the true solutions and will be updated in the process of iterations. Especially for high-order Godunov-based scheme, the solution of the first-order Godunov-based scheme is considered as the initial guess.

Step 2 (Alternating Sweepings): we compute $z_{i,j}^{\text{new}}$ according to the update formulation (24) or (29) by Gauss-Seidel iterations with four alternating direction sweepings:

(1) $i = 1{:}\ I$, $j = 1{:}\ J$;
(2) $i = I{:}\ 1$, $j = 1{:}\ J$;
(3) $i = I{:}\ 1$, $j = J{:}\ 1$;
(4) $i = 1{:}\ I$, $j = J{:}\ 1$.

Step 3 (Convergence): if $\|z^{\text{new}} - z^{\text{old}}\|_{L^1} \leq \mu$, where μ is a given threshold value, the schemes converge and stop; otherwise, return to Step 2. In this paper, we use $\mu = 10^{-5}$.

5. Experimental Results

Several experiments on synthetic and real images with different reflectance properties have been carried out in order to assess the effectiveness of the presented unified SFS approach. We compare our presented approach with the Ahmed and Farag's approach [24, 25] using Lax-Friedrichs sweeping scheme for the same reflectance property. We implement all the approaches in Matlab. All the experiments are conducted on a PC with a Xeon E5-1650 processor and 16 GB of DDR3 memory.

5.1. Experimental Results on Synthetic Images. We use two synthetic surfaces including a ball and a vase, which have been benchmark test surfaces and are determined by equations (30) and (31), respectively:

$$
z(x, y) = \sqrt{R^2 - \left(x^2 + y^2\right)},
\tag{30}
$$

where $R = 75$ is the radius of the ball and the generated image size $M \times N$ is 256×256; that is, $(x, y) \in [-127, 128] \times [-127, 128]$:

$$
z(x, y) = \sqrt{g(x)^2 - y^2},
\tag{31}
$$

where $g(x) = 0.15 - 0.025\,(6x - 1)\,(2x - 1)^2\,(3x + 2)^2\,(2x + 1)$ and original range of (x, y) values is $[-0.5, 0.5] \times [-0.5, 0.5]$. To obtain the same image size as the ball, we map (x, y) range to $[-127, 128]$ and scale $z(x, y)$ simultaneously. Their ground truths are shown in Figure 2.

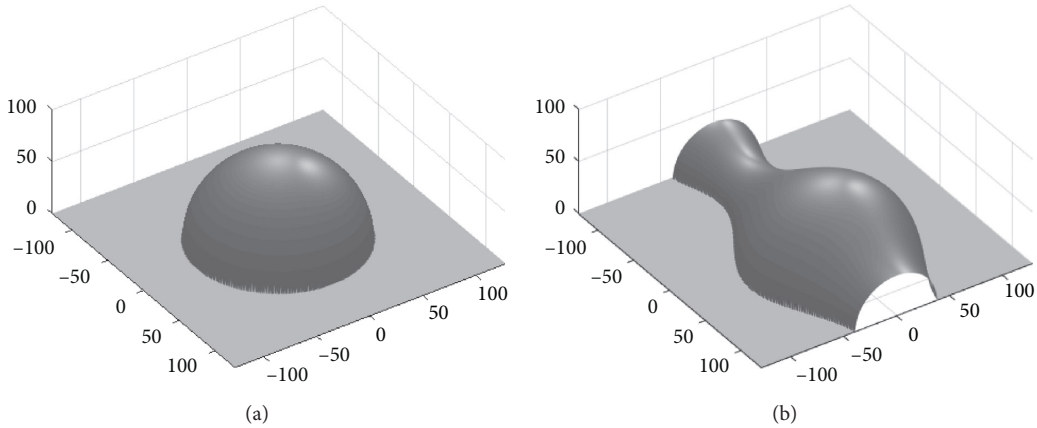

Figure 2: The ground truths of the ball and the vase surfaces. (a) The ball. (b) The vase.

In order to assess the effectiveness of the presented unified SFS approach for the surfaces of various reflectance properties, four different parameter sets of σ, w_d, w_s, and n are used to generate the shading images. Table 1 shows the parameter values. Especially for set (1) and set (2), $\sigma = 0$ means that the unified model reduces to the Blinn–Phong model with different diffuse and specular components, and for set (3), it means that the unified model reduces to the Oren–Nayar diffuse model.

The experimental results for the synthetic ball images are illustrated in Figure 3. Figures 3(a)–3(d) show the shading images generated by the four parameter sets shown in Table 1, respectively. Figures 3(e)–3(h) show the reconstructed surfaces of Figures 3(a)–3(d) using the first-order Godunov-based scheme, while Figures 3(i)–3(l) show the reconstructed surfaces using the high-order Godunov-based scheme. Finally, Figures 3(m)–3(p) show the reconstructed surfaces of Figures 3(a)–3(d) using the Lax-Friedrichs sweeping scheme. Figure 4 illustrates the corresponding experimental results for the synthetic vase images.

As can be roughly seen from Figures 3 and 4, the fast eikonal solvers and the Lax-Friedrichs sweeping scheme can basically get satisfactory reconstructed results for the four different parameter sets of the unified reflectance model. Furthermore, we can easily see that the first- and high-order Godunov-based schemes illustrate similar results, and both schemes can give much better reconstructed results with smaller differences between reconstructed surfaces and ground truths than the Lax-Friedrichs sweeping scheme, especially for more specular components such as Figures 3(b), 3(d), 4(b), and 4(d).

The effectiveness of our presented unified approach is further described by comparisons between the fast eikonal solvers and the Lax-Friedrichs sweeping scheme with the mean absolute (MA) error, the root mean square (RMS) error, and the CPU running time. Tables 2 and 3 list the quantitative comparisons of the three schemes for the synthetic ball and vase images. It can be seen obviously that the first-order Godunov-based scheme shows much more superiority in CPU running time in all the images that we carried out since it converges after about 2 iterations. At the same time, we can see that the high-order Godunov-based scheme exhibits the minimal reconstructed error in both the MA and RMS errors because the third-order weighted essentially nonoscillatory scheme is adopted in the approximation process. The Lax-Friedrichs sweeping scheme shows a worse performance; maybe, it is difficult to look for a perfect estimate for the artificial viscosity term.

5.2. Experimental Results on Real Images. In order to demonstrate the performance of our presented approach for real surface, we test it on two real images and also compare the reconstructed results with the Lax-Friedrichs sweeping scheme. The first image is a vase applied in [7], which is illustrated in Figure 5(a) and is mostly diffuse. The second image is a plastic bottle, which is illustrated in Figure 6(a) and contains more specular components. Figures 5(b) and 6(b) show the masks of Figures 5(a) and 6(a) representing the (x, y) that is used in reconstruction, respectively. Figures 5(c)–5(e) illustrate the reconstructed surfaces using the first-order Godunov-based scheme, the high-order Godunov-based scheme, and the Lax-Friedrichs sweeping scheme, respectively. Figures 6(c)–6(e) show the corresponding reconstructed surfaces for the bottle.

We only evaluate the effectiveness intuitively and qualitatively. From the reconstructed results shown in Figures 5(c)–5(e), we can see that the fast eikonal solvers are more accurate than the Lax-Friedrichs sweeping scheme for mostly diffuse surface. Details of surfaces illustrated in Figures 5(c) and 5(d) are represented more vividly and clearly than in Figure 5(e). From the reconstructed results shown in Figures 6(c)–6(e), we can draw the similar conclusions as for more specular surface. As shown previously, from Figures 5(e) and 6(e), we can see that the Lax-Friedrichs sweeping scheme also exhibits a slightly worse performance since it is hard to find a perfect estimate for the artificial viscosity term. It is well worth noting that the first-order Godunov-based scheme is the fastest and the reconstructed surface using the high-order Godunov-based scheme looks like the best result.

Table 1: Parameter values employed to generate the shading images.

Parameter	σ	w_d	w_s	n
Set (1)	0	0.8	0.2	5
Set (2)	0	0.5	0.5	10
Set (3)	0.3	1	0	—
Set (4)	0.3	0.5	0.5	10

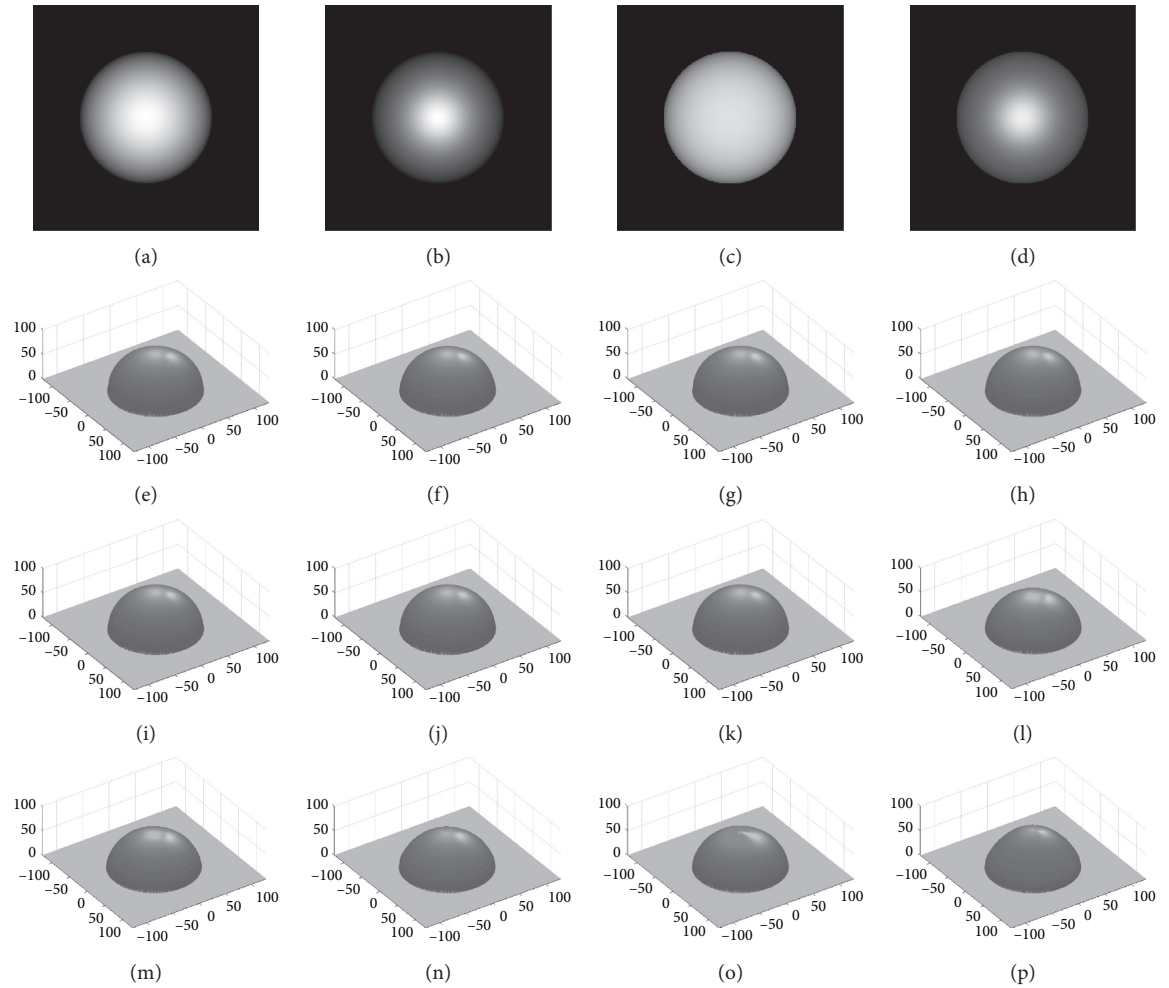

Figure 3: Experimental results for the synthetic ball images. (a)–(d) The shading images generated by the four parameter sets shown in Table 1. (e)–(h) Reconstructed surfaces of (a)–(d) using first-order Godunov-based scheme. (i)–(l) Reconstructed surfaces of (a)–(d) using high-order Godunov-based scheme. (m)–(p) Reconstructed surfaces of (a)–(d) using Lax-Friedrichs sweeping scheme.

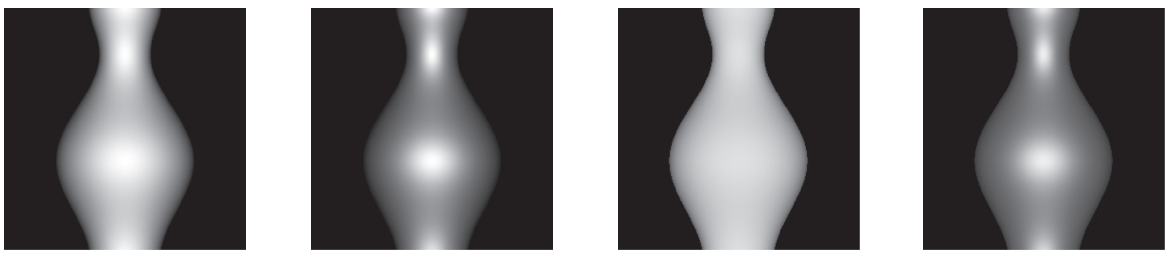

Figure 4: Continued.

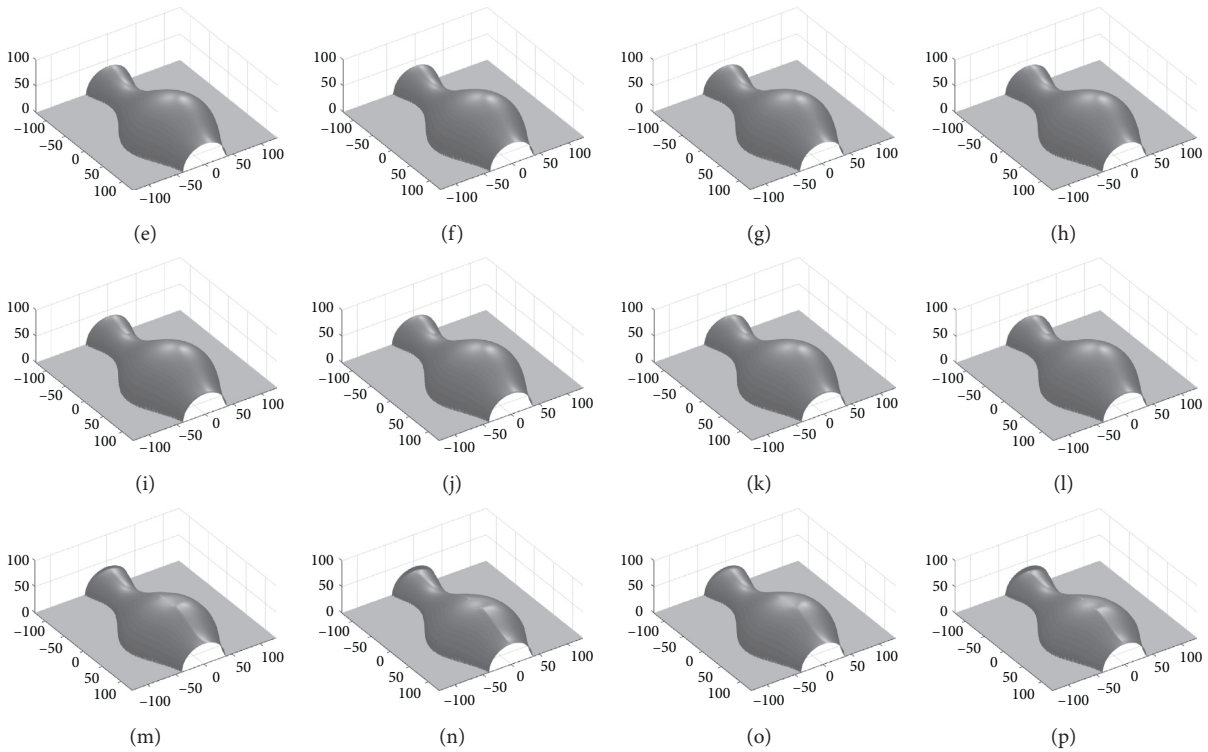

Figure 4: Experimental results for the synthetic vase images. (a)–(d) The shading images generated by the four parameter sets shown in Table 1. (e)–(h) Reconstructed surfaces of (a)–(d) using first-order Godunov-based scheme. (i)–(l) Reconstructed surfaces of (a)–(d) using high-order Godunov-based scheme. (m)–(p) Reconstructed surfaces of (a)–(d) using Lax-Friedrichs sweeping scheme.

Table 2: Quantitative comparisons of schemes for the synthetic ball images.

Images	First-order Godunov-based scheme			High-order Godunov-based scheme			Lax-Friedrichs sweeping scheme		
	MA	RMS	Time (s)	MA	RMS	Time (s)	MA	RMS	Time (s)
Figure 3(a)	0.7199	0.8924	0.04	0.0370	0.0883	0.64	3.2049	3.3360	2.49
Figure 3(b)	0.7228	0.9176	0.04	0.0595	0.1318	0.65	3.9782	4.1671	3.69
Figure 3(c)	0.7167	0.8902	0.04	0.0357	0.0725	0.64	2.6534	2.7687	2.67
Figure 3(d)	0.7776	1.0667	0.04	0.0940	0.1959	0.65	4.1396	4.3401	5.07

Table 3: Quantitative comparisons of schemes for the synthetic vase images.

Images	First-order Godunov-based scheme			High-order Godunov-based scheme			Lax-Friedrichs sweeping scheme		
	MA	RMS	Time (s)	MA	RMS	Time (s)	MA	RMS	Time (s)
Figure 4(a)	0.5770	0.7129	0.04	0.0740	0.1371	0.81	2.2899	2.5879	2.31
Figure 4(b)	0.5791	0.7284	0.04	0.0812	0.1429	0.82	3.5141	3.8832	3.53
Figure 4(c)	0.5739	0.7095	0.04	0.0731	0.1366	0.81	1.3744	1.6557	3.61
Figure 4(d)	0.6309	0.7429	0.04	0.0953	0.1550	0.82	4.0818	4.4402	4.82

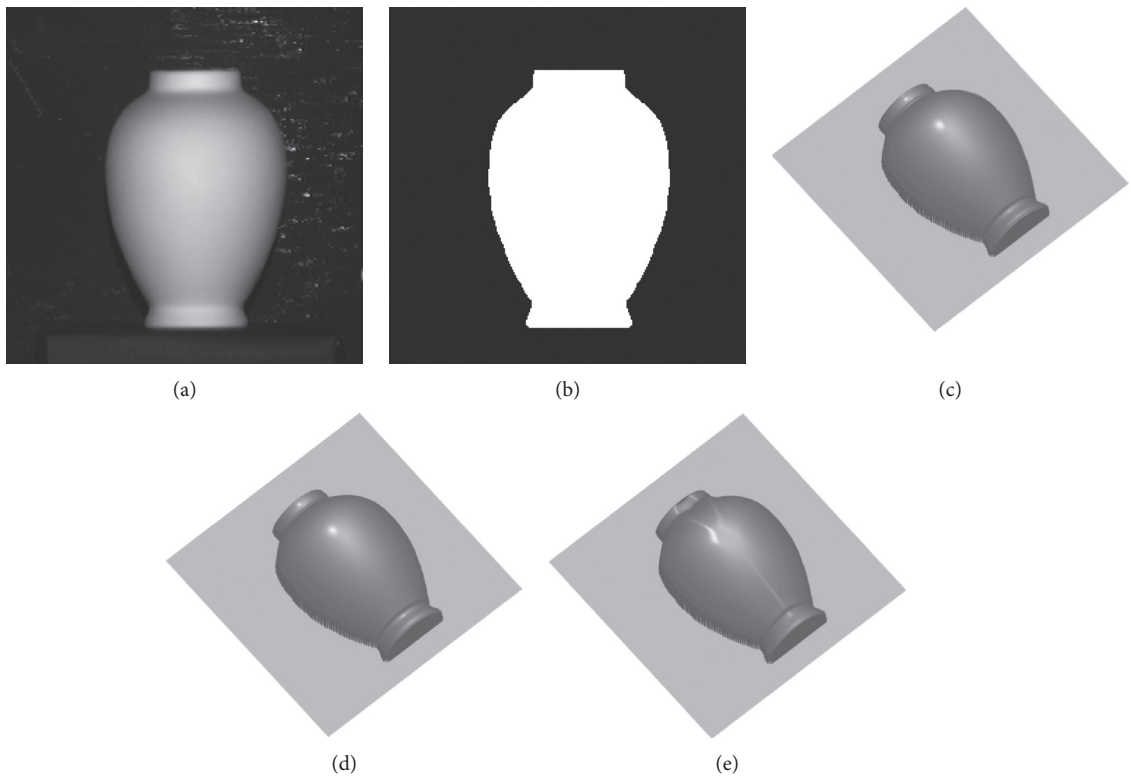

Figure 5: Experimental results for the real vase image. (a) The real image. (b) The mask of (a). (c) Reconstructed surface of (a) using first-order Godunov-based scheme. (d) Reconstructed surface of (a) using high-order Godunov-based scheme. (e) Reconstructed surface of (a) using Lax–Friedrichs sweeping scheme.

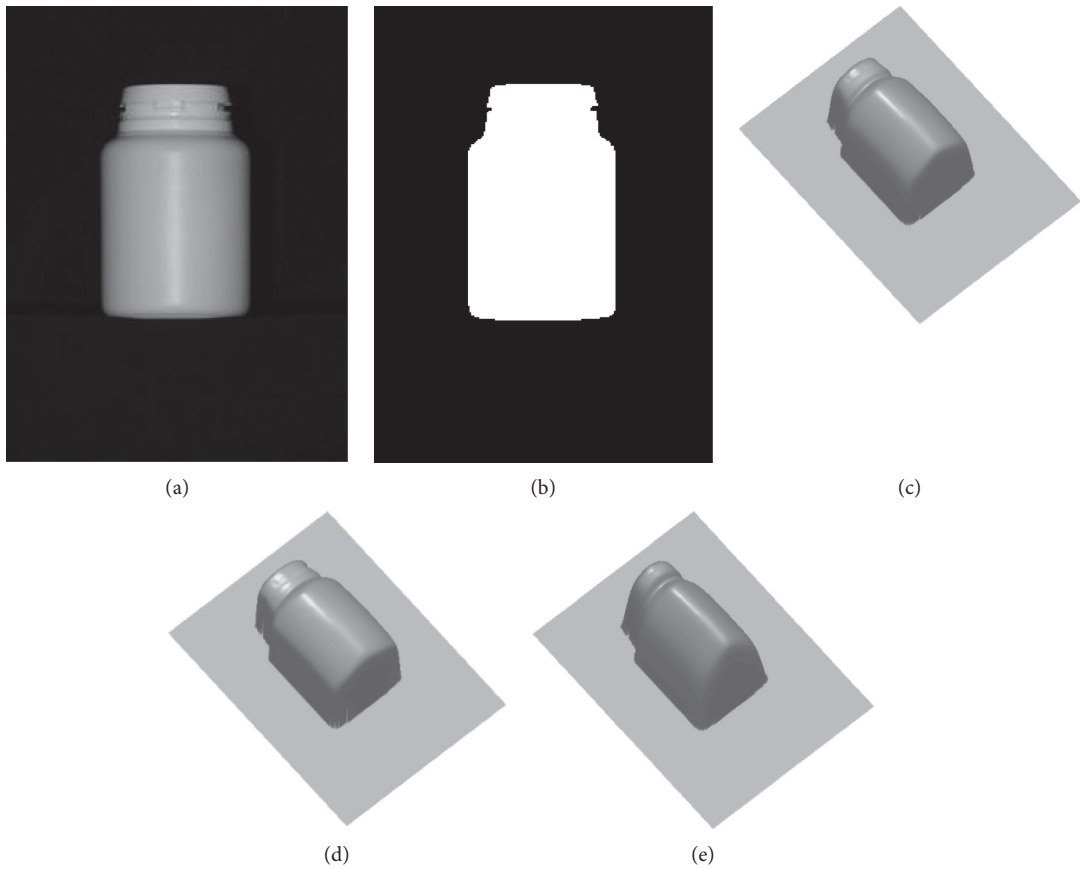

Figure 6: Experimental results for the real bottle image. (a) The real image. (b) The mask of (a). (c) Reconstructed surface of (a) using first-order Godunov-based scheme. (d) Reconstructed surface of (a) using high-order Godunov-based scheme. (e) Reconstructed surface of (a) using Lax–Friedrichs sweeping scheme.

6. Conclusions

In this paper, we have reported a unified SFS approach for surfaces of various reflectance properties including diffuse, specular, and hybrid reflections using fast eikonal solvers. A unified reflectance model that is a linear combination of the Oren–Nayar model and the specular part of the Blinn–Phong model is presented. We have derived the unified image irradiance equation under this unified model with an orthographic camera projection and a single distant point light source whose direction is the same as the camera. We have also converted the PDII equation into an eikonal-type PDE through solving a high-order equation by using the Newton-Raphson method. Fast eikonal solvers which are comprised of the first- and high-order Godunov-based schemes accelerated by the fast sweeping method are employed to solve the viscosity solution of the resultant eikonal-type PDE. Finally, the experiments are conducted on both synthetic and real images and the results verify that our presented approach can provide satisfactory 3D surface reconstruction with a higher accuracy in less CPU running time.

Frankly speaking, the presented unified SFS approach can only handle the special case which assumes an orthographic camera projection and a single distant point light source whose direction is parallel to the optical axis of the camera lens. In future work, we will adopt the idea of using the Newton-Raphson method to solve the high-order PDII equations derived from the SFS problem with a more complex reflectance model and will relax the two assumptions by employing a nearby point light source and a perspective camera projection. The attenuation term of the light illumination will be also considered to eliminate the convex-concave ambiguity which can make the SFS problem ill-posed.

Data Availability

The data used to support the findings of this study are included within the article.

Conflicts of Interest

The authors declare that they have no conflicts of interest.

Acknowledgments

The work in this paper is supported by the Open Fund of Shaanxi Province key Laboratory of Photoelectricity Measurement and Instrument Technology, Xi'an Technological University (no. 2016SZSJ-60-1) and Xi'an Key Laboratory of Intelligent Detection and Perception (no. 201805061ZD12CG45).

References

[1] E. Prados and O. Faugeras, "A generic and provably convergent shape-from-shading method for orthographic and pinhole cameras," *International Journal of Computer Vision*, vol. 65, no. 1-2, pp. 97–125, 2005.

[2] J.-F. Hu, W.-S. Zheng, X. Xie, and J. Lai, "Sparse transfer for facial shape-from-shading," *Pattern Recognition*, vol. 68, pp. 272–285, 2017.

[3] G. Wang, J. Han, and X. Zhang, "Three-dimensional reconstruction of endoscope images by a fast shape from shading method," *Measurement Science and Technology*, vol. 20, no. 12, Article ID 125801, 2009.

[4] Y. C. Ju, S. Tozza, M. Breuß, A. Bruhn, and A. Kleefeld, "Generalised perspective shape from shading with Oren-Nayar reflectance," in *Proceedings of the British Machine Vision Conference (BMVC)*, pp. 42.1–42.11, Bristol, UK, September 2013.

[5] B. K. P. Horn, *Shape from shading: a method for obtaining the shape of a smooth opaque object from one view*, Ph.D. thesis, Massachusetts Institute of Technology, Cambridge, MA, USA, 1970.

[6] W. C. Liu, B. Wu, and C. Wöhler, "Effects of illumination differences on photometric stereo shape-and-albedo-from-shading for precision lunar surface reconstruction," *ISPRS Journal of Photogrammetry and Remote Sensing*, vol. 136, pp. 58–72, 2018.

[7] R. Zhang, P.-S. Tsai, J. E. Cryer, and M. Shah, "Shape from shading: a survey," *IEEE Transactions on Pattern Analysis and Machine Intelligence*, vol. 21, no. 8, pp. 690–706, 1999.

[8] J.-D. Durou, M. Falcone, and M. Sagona, "Numerical methods for shape-from-shading: a new survey with benchmarks," *Computer Vision and Image Understanding*, vol. 109, no. 1, pp. 22–43, 2008.

[9] G. Wang and J. Cheng, "Three-dimensional reconstruction of hybrid surfaces using perspective shape from shading," *Optik*, vol. 127, no. 19, pp. 7740–7751, 2016.

[10] S. Tozza and M. Falcone, "Analysis and approximation of some shape-from-shading models for non-Lambertian surfaces," *Journal of Mathematical Imaging and Vision*, vol. 55, no. 2, pp. 153–178, 2016.

[11] G. Wang and Y. Chu, "A new Oren-Nayar shape-from-shading approach for 3D reconstruction using high-order Godunov-based scheme," *Algorithms*, vol. 11, no. 5, p. 75, 2018.

[12] E. Rouy and A. Tourin, "A viscosity solutions approach to shape-from-shading," *SIAM Journal on Numerical Analysis*, vol. 29, no. 3, pp. 867–884, 1992.

[13] R. Kimmel and J. A. Sethian, "Optimal algorithm for shape from shading and path planning," *Journal of Mathematical Imaging and Vision*, vol. 14, no. 3, pp. 237–244, 2001.

[14] L. Governi, R. Furferi, L. Puggelli, and Y. Volpe, "A practical approach based on shape from shading and fast marching for 3D geometry recovery under oblique illumination," *Applied Mechanics and Materials*, vol. 472, pp. 503–509, 2014.

[15] M. Breuss, E. Cristiani, J.-D. Durou, M. Falcone, and O. Vogel, "Numerical algorithms for perspective shape from shading," *Kybernetika*, vol. 46, no. 2, pp. 207–225, 2010.

[16] M. Breuss, E. Cristiani, J.-D. Durou, M. Falcone, and O. Vogel, "Perspective shape from shading: ambiguity analysis and numerical approximations," *SIAM Journal on Imaging Sciences*, vol. 5, no. 1, pp. 311–342, 2012.

[17] J. A. Sethian, "Fast marching methods," *SIAM Review*, vol. 41, no. 2, pp. 199–235, 1999.

[18] K. Ikeuchi and B. K. P. Horn, "Numerical shape from shading and occluding boundaries," *Artificial Intelligence*, vol. 17, no. 1–3, pp. 141–184, 1981.

[19] A. Tankus, N. Sochen, and Y. Yeshurun, "A new perspective [on] shape-from-shading," in *Proceedings of the 9th IEEE International Conference on Computer Vision (ICCV)*, pp. 862–869, Nice, France, October 2003.

[20] H. Santo, M. Samejima, and Y. Matsushita, "Numerical shape-from-shading revisited," *IPSJ Transactions on Computer Vision and Applications*, vol. 10, no. 1, p. 8, 2018.

[21] Y. Quéau, J. Mélou, F. Castan, D. Cremers, and J.-D. Durou, "A variational approach to shape-from-shading under natural illumination," in *Proceedings of the International Workshop on Energy Minimization Methods in Computer Vision and Pattern Recognition (EMMCVPR)*, pp. 342–357, Venice, Italy, November 2017.

[22] M. Oren and S. K. Nayar, "Generalization of the Lambertian model and implications for machine vision," *International Journal of Computer Vision*, vol. 14, no. 3, pp. 227–251, 1995.

[23] H. Ragheb and E. R. Hancock, "Surface radiance correction for shape from shading," *Pattern Recognition*, vol. 38, no. 10, pp. 1574–1595, 2005.

[24] A. H. Ahmed and A. A. Farag, "Shape from shading for hybrid surfaces," in *Proceedings of the 2007 IEEE International Conference on Image Processing (ICIP)*, pp. 525–528, San Antonio, TX, USA, September 2007.

[25] A. H. Ahmed and A. A. Farag, "Shape from shading under various imaging conditions," in *Proceedings of the 2007 IEEE Conference on Computer Vision and Pattern Recognition (CVPR)*, pp. 1–8, Minneapolis, MN, USA, June 2007.

[26] C. Y. Kao, S. Osher, and J. Qian, "Lax-Friedrichs sweeping scheme for static Hamilton-Jacobi equations," *Journal of Computational Physics*, vol. 196, no. 1, pp. 367–391, 2004.

[27] O. Vogel and E. Cristiani, "Numerical schemes for advanced reflectance models for shape from shading," in *Proceedings of the 2011 IEEE International Conference on Image Processing (ICIP)*, pp. 5–8, Brussels, Belgium, September 2011.

[28] S. Tozza and M. Falcone, "A semi-Lagrangian approximation of the Oren-Nayar PDE for the orthographic shape-from-shading problem," in *Proceedings of the 2014 International Conference on Computer Vision Theory and Applications (VISAPP)*, pp. 711–716, Lisbon, Portugal, January 2014.

[29] B. T. Phong, "Illumination for computer generated pictures," *Communications of the ACM*, vol. 18, no. 6, pp. 311–317, 1975.

[30] S. Galliani, Y. C. Ju, M. Breuss, and A. Bruhn, "Generalised perspective shape from shading in spherical coordinates," in *Proceedings of the 4th International Conference on Scale Space and Variational Methods in Computer Vision (SSVM)*, pp. 222–233, Leibnitz, Austria, June 2013.

[31] F. Camilli and S. Tozza, "A unified approach to the well-posedness of some non-Lambertian models in shape-from-shading theory," *SIAM Journal on Imaging Sciences*, vol. 10, no. 1, pp. 26–46, 2017.

[32] J. F. Blinn, "Models of light reflection for computer synthesized pictures," *ACM SIGGRAPH Computer Graphics*, vol. 11, no. 2, pp. 192–198, 1977.

[33] H.-K. Zhao, "A fast sweeping method for Eikonal equations," *Mathematics of Computation*, vol. 74, no. 250, pp. 603–627, 2005.

[34] Y.-T. Zhang, H.-K. Zhao, and J. Qian, "High order fast sweeping methods for static Hamilton-Jacobi equations," *Journal of Scientific Computing*, vol. 29, no. 1, pp. 25–56, 2006.

[35] Y.-H. R. Tsai, L.-T. Cheng, S. Osher, and H.-K. Zhao, "Fast sweeping algorithms for a class of Hamilton-Jacobi equations," *SIAM Journal on Numerical Analysis*, vol. 41, no. 2, pp. 673–694, 2003.

[36] G.-S. Jiang and D. Peng, "Weighted ENO schemes for Hamilton-Jacobi equations," *SIAM Journal on Scientific Computing*, vol. 21, no. 6, pp. 2126–2143, 2000.

Hindawi
International Journal of Optics
Volume 2020, Article ID 6712781, 13 pages
https://doi.org/10.1155/2020/6712781

Research Article

Three-Dimensional Reconstruction of Mechanical Parts Based on Digital Holography

Yaohui Dai, Haiyu Wu, Gang Zhu, and Yan Yang

College of Mechanical Engineering, Chongqing University of Technology, Chongqing 400054, China

Correspondence should be addressed to Yan Yang; yangyan@cqut.edu.cn

Received 3 November 2019; Revised 7 February 2020; Accepted 4 March 2020; Published 1 May 2020

Guest Editor: Changsoo Je

In reconstruction of the off-axis digital hologram of diffuse reflection objects, the position of the positive first-order image cannot be accurately obtained because of the low quality of the reconstruction image. This paper focuses on the above problem and proposes a method for marking the first-order image of the 1-FFT surface based on the fast Fourier transform (1-FFT). The parameters of angle of illumination light were investigated, and the maximum relative measurement error is 5.6% by standard objects. The multiaperture stitching technique in cylindrical coordinates is applied to digital holography technology, and the particle swarm optimization algorithm is used to transform the nonlinear equations into optimization problems to solve the splicing parameters. Finally, the 3D display of a typical rotary three-dimensional mechanical part is successfully realized with holography stitching using the above method.

1. Introduction

With the development of computers and charge-coupled devices (CCDs), the three-dimensional object display based on digital holography has also been developed accordingly. Some convention optical methods of obtaining three-dimensional contours of objects are proposed which include grating projection method and optical knife scanning method [1–3]. These methods have their own shortcomings, such as the need for a projection system or a scanning system. In contrast, the advantages of digital holography are obvious. Digital holography does not require a cumbersome process such as film processing as in the conventional one and quantitatively obtains the phase information of the object, which can obtain the three-dimensional contour of the object. Yamaguchi et al. [4,5] obtained the three-dimensional contour of the object by using phase-shifted digital holography. This method eliminates conjugate images and zero-order images and can measure millimeter-level objects, but this method requires a high degree of environmental stability and requires a high-precision phase shifter. In digital holography, the dual light source method is used to make a slight change in the angle of the illumination light [6–9] and obtain the three-dimensional contour of the object by calculating the phase difference between the reconstructed images before and after. However, during the current measurement process, there are two main problems: (1) the reconstruction image of a weak diffusely reflecting object has poor contrast because of its low light intensity. It is difficult to accurately locate the positive first-order image of the object on the reconstructed image plane, which affects the subsequent acquisition of the interference phase map. (2) The imaging angle is limited and influenced by the size of the CCD array and the total number of pixels, so some additional methods are needed to achieve the fusion of the multiview contour.

The off-axis digital holographic reconstruction process of diffuse reflection objects is studied in this paper. Aiming at the problem that the intensity of the light emitted by the weak diffuse reflection object is low, the contrast is poor, and the position of the positive first-order image of the object in the reconstruction plane cannot be accurately located, and a premarking method of the reconstructed image position for diffusely reflecting objects is proposed. Combining of changing the inclination of the illumination light and the filtering-image of 4 times fast Fourier transform

(FIMG4FFT) method [10], the three-dimensional contour of the object at a specific perspective is obtained. A calibration target with a height difference of 9 mm is used in demonstration test. The results show that the measurement error is between 0.1 mm and 0.5 mm. The maximum relative measurement error is 5.6%. The multiaperture stitching technique in cylindrical coordinates is applied to accomplish the digital holographic 3D stitching. The particle swarm optimization algorithm is used to transform the nonlinear equations into optimization problems to solve the splicing parameters. The contour from a single viewpoint is stitched together to realize the three-dimensional display of the whole object. Finally, the three-dimensional stitching of rotational three-dimensional objects in the cylindrical coordinate system is carried out, and the experiment has been verified.

2. Principles

2.1. Principle of the Inclined Illumination Method. Li and Peng [11] derived the basic formula for three-dimensional shape detection based on digital holography. Figure 1 shows the measurement principle of the digital holographic three-dimensional topography measurement. In Cartesian coordinates $Oxyz$, the plane of $z=0$ is defined as the reconstructed plane, which is parallel to the CCD window plane with a distance of $z = d_1$ and tangent to the surface of the measured object.

According to the statistical optics theory [12], the nonoptically smooth spatial surface is illuminated with coherent light, and the scattered light field of the surface of the object can be regarded as the scattered light of a large number of scattering primitives, that is, the superposition of all primitive scattering waves. The reconstructed light wave field of the entire object in the $z = 0$ plane can be expressed as [13]

$$O(x, y, 0) = C_R o(x, y, z)\exp[j\phi(x, y, z) + j\phi_r - jkz]. \tag{1}$$

In formula (1), $|C_R o(x, y, z)|^2$ denotes the intensity of diffuse reflected light at the corresponding points on the surface of an object because the intensity information of the object is not mainly concerned here, so it is not discussed here. $j = \sqrt{-1}$ and $k = 2\pi/\lambda$, λ are the wavelengths of light, ϕ_r denotes the random phase, the range of variation is $-\pi$: π, and z is the reconstruction distance.

If the direction of illumination in Figure 1 is parallel to xoz and the angle between illumination and axis z is θ, the phase can be expressed as

$$\phi(x, y, z) = \frac{2\pi}{\lambda}(x\sin\theta - z\cos\theta). \tag{2}$$

In formula (2), θ is the illumination light tilt angle. Studying the absolute phase measurement shows that if one wavelength is used to illuminate, the projection angle can be changed to obtain two reconstructed fields and then superimposed to form a contour line, which realizes the measurement of the three-dimensional shape.

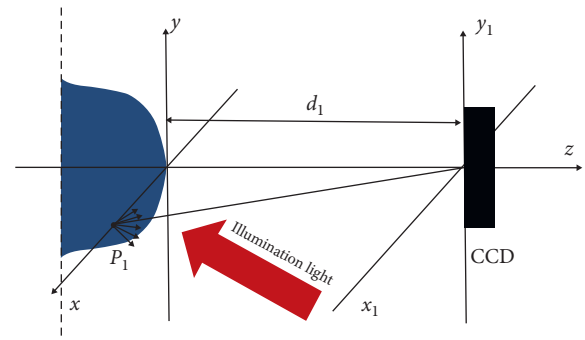

Figure 1: Schematic diagram of the tilt illumination method.

According to formula (2), when the light wave with wavelength λ illuminates the object with parallel illumination with inclination angle of illumination light θ and $\theta + \Delta\theta$, the phase distributions of the light field in the reconstructed object plane are, respectively,

$$\phi_1(x, y) = \frac{2\pi}{\lambda}[x\sin\theta - z(1 + \cos\theta)] + \phi_{r1}, \tag{3}$$

$$\phi_2(x, y) = \frac{2\pi}{\lambda}\{x\sin(\theta + \Delta\theta) - z[1 + \cos(\theta + \Delta\theta)]\} + \phi_{r2}. \tag{4}$$

In formulas (3) and (4), all ϕ_{r1}, ϕ_{r2} denote the random phase of $-\pi$: π with uniform probability.

Subtract the two formulas:

$$\phi_1(x, y) - \phi_2(x, y) = \frac{2\pi}{\lambda}\{x[\sin\theta - (\theta + \Delta\theta)] - z[\cos\theta - \cos(\theta + \Delta\theta)]\} + \phi_{r1} - \phi_{r2}. \tag{5}$$

When $\Delta\theta$ is very small, it can be seen that the same light wave irradiates on the surface of the object, and the scattering characteristics of the same light wave on the surface of the object do not change too much. At this time, $\phi_{r1} - \phi_{r2}$ is no longer the random phase of $-\pi$: π with uniform value probability. Because $\Delta\theta$ is relatively small, so $\cos\Delta\theta \approx 1$, $\sin\Delta\theta \approx \Delta\theta$ and $\phi_{r1} - \phi_{r2} = \varepsilon 2\pi\,(0 < \varepsilon < 1)$, which are phase measurement noises, and formula (5) can be rewritten:

$$\Delta\phi(x, y) = \frac{2\pi}{\lambda}(-x\Delta\theta\cos\theta - z\Delta\theta\sin\theta) + \varepsilon 2\pi. \tag{6}$$

Formula (6) shows that the phase difference is composed of two parts. The latter is highly correlated with the surface of the object. The former is linearly related to the spatial coordinate x, called the linear tilt term. The change in its value is accompanied by a change in its coordinate value. The phase difference is caused by its changes much more dramatically than that caused by the height change of the object itself, which makes the phase difference $\Delta\phi$ wrapped seriously. In this way, the phase difference image of the object can be obtained by removing the linear tilt term before phase unwrapping. Formula (6) is after denoising, and the height of the surface of the object varies with the coordinates, which can be written as follows:

$$z(x,y) \approx -\frac{\Delta\phi(x,y)}{2\pi}\Lambda_\theta - x\cot\theta,$$
$$\Lambda_\theta = \frac{\lambda}{\Delta\theta\sin\theta}. \tag{7}$$

Λ_θ represents the change in the height of the object corresponding to the change in phase difference of 2π, and it can be seen that it is inversely proportional to the system sensitivity. When Λ_θ is greater than or equal to the maximum depth measured on the surface, the phase diagram cannot be wrapped.

2.2. FIMG4FFT Wavefront Reconstruction Method. According to the scalar diffraction theory [14] and the paraxial approximation of diffraction, Fresnel diffraction integral is often used in wavefront reconstruction of digital holography. Fresnel diffraction integral can be divided into two forms: Fourier transform and convolution. When Fourier transform is used, it can be calculated by one-time fast Fourier transform (FFT). This method is called 1-FFT method for short, but when reconstruction is performed by the 1-FFT method, the area of the reconstructed digital hologram image is smaller [15]. In order to obtain a high-quality reconstructed image and make the image of the selected area of the object be displayed on the reconstructed plane completely, so that the interference phase with high quality can be obtained later, the image plane filtering technology [16] is used to reconstruct the digital holographic image in 1-FFT, which is not interfered by other factors. To ensure that the resolution of the reconstructed image is as large as the original hologram, it is necessary to use zero-filling operation around the image. Then, inverse diffraction operation is to make the digital hologram free from interference on the object plane, and then it uses the spherical wave as the reconstruction wave to irradiate, and it uses the angular spectrum diffraction method to reconstruct the high-quality digital hologram reconstruction image. This method requires four FFT calculations (FIMG4FFT method for short) [17–19].

In the digital holographic recording system, there is a Cartesian coordinate system $Oxyz$, the $z = 0$ plane where the hologram is located, the distance of the object plane from the hologram plane is z_0, and the digital hologram obtained by CCD recording is $I(x, y)$; then, the 1-FFT reconstruction light wave field can be expressed by the following Fresnel diffraction integral [14]:

$$U(x,y) = \frac{\exp(jkz_0)}{j\lambda z_0}\exp\left[\frac{jk}{2z_0}\left(x_i^2 + y_i^2\right)\right] \times \int_{-\infty}^{+\infty}\int_{\infty}^{\infty}\left\{I(x,y)\exp\left[\frac{jk}{2z_0}\left(x^2+y^2\right)\right]\right\} \cdot \exp\left[-j2\pi\left(\frac{x_i}{\lambda z_0}x + \frac{y_i}{\lambda z_0}y\right)\right]\mathrm{d}x\mathrm{d}y. \tag{8}$$

In formula (8), λ is the wavelength of the light wave and $k = 2\pi/\lambda$.

The reconstructed spherical wave with a radius of z_c is used to illuminate the reconstructed image:

$$R_c(x,y) = \exp\left[\frac{jk}{2z_c}\left(x^2+y^2\right)\right]. \tag{9}$$

The light wave field of the undisturbed digital hologram propagating through distance z_i is as follows:

$$U_i(x,y) = FFT^{-1}\left\{FFT\left[w(x,y)U^*(x,y)R_c(x,y)\right] \cdot \exp\left[jkz_i\sqrt{1-\lambda^2\left(f_x^2+f_y^2\right)}\right]\right\}. \tag{10}$$

In formula (10), $\omega(x, y)$ denotes the window function of the hologram, $U^*(x, y)$ denotes the object field in the $z = 0$ plane corresponding to the local image of the selected object on the image plane, and f_x, f_y denote the frequency coordinates corresponding to x, y.

In the above formula, if the reconstruction distance z_i is satisfied,

$$z_i = \left(\frac{1}{z_0} - \frac{1}{z_c} - \frac{1}{z_r}\right)^{-1}. \tag{11}$$

In formula (11), z_r is the reference wave surface radius. The reconstructed image of the object field whose magnification is $M = z_1/z_0$ is obtained by angular spectrum diffraction formula (10).

In the off-axis digital holographic reconstruction system, there are two basic conditions that must be met. One is Nyquist sampling theories; another is the positive and negative first-order image separation conditions [19]. When these two conditions are met, the positive first-order image in the digital hologram will be able to reconstruct. The marking method of the positive first-order image of the 1-FFT surface is based on these two conditions. The marking method is as follows. Taking the virtual nut as the measured object is shown in Figure 2.

First, the surface of the nut mainly based on specular reflection is recorded in CCD, and the position of the positive first-order image on the 1-FFT surface is adjusted to separate the positive and negative first-order images from the zero-order image; after that operation, the position of the first-order image on the 1-FFT surface is recorded. The hologram process captured by mirror reflected light is shown in Figure 2(a).

Then, rotate the nut slightly without changing its position so that the mirror reflected light is far away from the CCD and the diffuse reflected light from the nut enters the CCD. The hologram process captured by diffuse reflection light is shown in Figure 2(b). Because the nut is fixed on the rotating table, it only rotates, and its spatial position does not change, so the angle of the reference light does not change, so the diffuse reflection image can be obtained at the same position on the 1-FFT reconstruction image plane.

2.3. Multiaperture Stitching Model in Cylindrical Coordinates. Rotary three-dimensional objects are not easy to express in Cartesian coordinates, and the range of the measured aperture is limited. The central angle of the maximum measurable surface cannot exceed 180 degrees. As shown in Figure 3, a

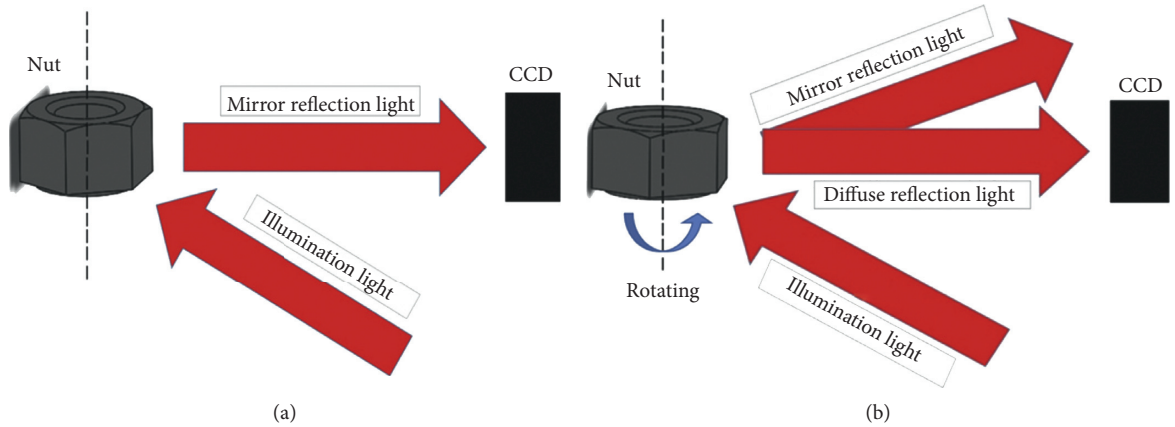

Figure 2: The marking method of the positive first-order image of the 1-FFT surface: (a) before the nut turns; (b) after the nut turns.

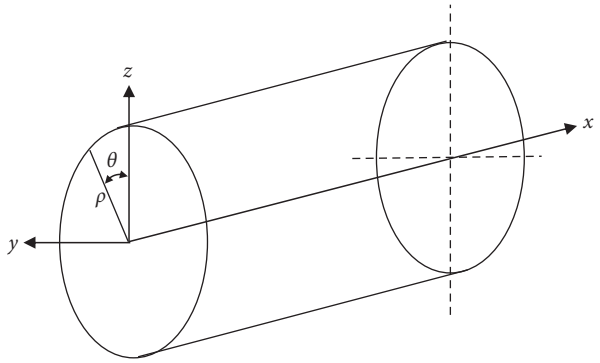

Figure 3: The transformation relationship between the cylindrical coordinate system and the Cartesian coordinate system.

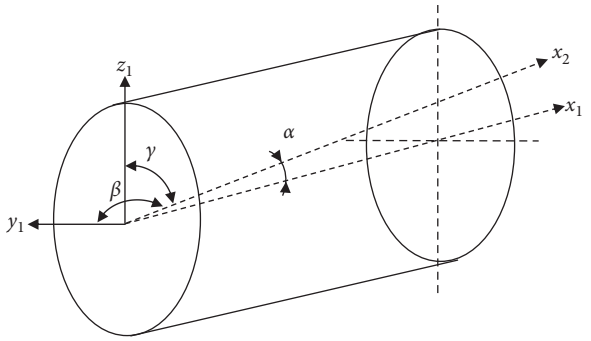

Figure 4: Two cylindrical coordinates with uncoincidental axes.

cylindrical coordinate system ($O\rho\theta x$) corresponds to a rectangular coordinate system ($Oxyz$). Assume that a point P in the space has a coordinate value $P(x, y, x)$ in a rectangular coordinate system and a corresponding coordinate value $P(\rho, \theta, x)$ in a cylindrical coordinate system. Among them, ρ is the vertical distance from point P to axis X, and θ is the angle between the projection of the vertical line from point P to axis X on the yoz plane and the Z-axis. The relationship between the two can be expressed as [20,21]

$$\begin{cases} \rho = \sqrt{y^2 + z^2}, \\ \tan\theta = \dfrac{z}{y}. \end{cases} \tag{12}$$

In both coordinate systems, the technology of multi-aperture stitching is coordinate transformation, but there is rotation between adjacent areas in the cylindrical coordinate system, so it is necessary to solve the least square solution of the nonlinear equations when it solves the relative position relationship between adjacent two viewpoints. When the object rotates, there are some motion errors in mechanical equipment, so when it moves from one perspective to the next one, there will be noncoincidence between adjacent overlapping areas, and then the coordinate origin and axis will be offset. The coordinate axes do not coincide, as shown in Figure 4, which indicates that the axis of the second coordinate system X_2 is cosine ($\cos\alpha$, $\cos\beta$, $\cos\gamma$) with respect to the direction of the first coordinate system, and the coordinate origins do not coincide as shown in Figure 5.

To investigate this offset, when two circular surfaces are projected in the above coordinate system onto a plane where x is constant, which are two circles with different circle centers, the distance between the centers of the two circles can be expressed as

$$\rho_0' = \sqrt{\left(\rho_0 \sin\theta_0 + \frac{\cos\beta}{\cos\alpha}x_1\right)^2 + \left(\rho_0 \cos\theta_0 + \frac{\cos\gamma}{\cos\alpha}x_1\right)^2}. \tag{13}$$

The orientation between the centers of the two circles is

$$\theta_0' = \arctan\left(\frac{\rho_0 \sin\theta_0 + (\cos\beta/\cos\alpha)x_1}{\rho_0 \cos\theta_0 + (\cos\gamma/\cos\alpha)x_1}\right). \tag{14}$$

In formula (14), ρ_0 and θ_0 denote the distance and orientation between two cylinders on the plane of $x_1 = 0$ and the centers of two circles formed by the intersection of the two cylinders on the plane, as shown in Figure 5.

According to the overlapping area between two sub-apertures and the geometric relationship between the cylindrical coordinate systems, the transformation relationship between the two coordinate systems can be obtained as follows:

$$\begin{cases} \rho_1 = \sqrt{\rho_2^2 + \rho_2^{'2} - 2\rho_2\rho_0' \cos\left(\theta_2 - \theta_0' - \varphi\right)}, \\ \theta_1 = \sin^{-1}\left[\left(\dfrac{\rho_0'}{\rho_1}\right)\sin\left(\theta_0' - \theta_2 - \varphi\right)\right] + \theta_2 + \varphi, \\ \rho_1 = f\left(\theta_1, x_1\right). \end{cases} \tag{15}$$

In formula (15), φ is the angle of rotation around the X_1-axis between two coordinate systems. ρ_0, θ_0 and any two of the direction cosines $(\cos\alpha, \cos\beta, \cos\gamma)$ (due to $\cos^2\alpha + \cos^2\beta + \cos^2\gamma = 1$) can represent the relative positional relationship of the two measurement angles in their respective coordinate systems. Because there are four unknowns, four points can be solved in the overlapping region. However, in order to reduce the influence of noise, several points of the overlapping region are usually substituted into equation (14) to form a nonlinear equation group, and by solving the least square solution, we can get the parameters ρ_0, θ_0 and direction cosine $(\cos\alpha, \cos\beta, \cos\gamma)$. Then, we can transfer the measurement results from different angles of view, i.e., local coordinates into the global coordinate system by coordinate transformation to achieve the purpose of multiview stitching.

The splicing model in cylindrical coordinates is suitable for the measurement of rotating parts, but the main disadvantage of this model is that the equations are severely nonlinear, which makes the solving process complicated. On the basis of preserving the above advantages, to simplify the process, this paper adopts the multiaperture splicing technique in the cylindrical coordinate system based on the particle swarm optimization algorithm, which converts the nonlinear problem into an optimization problem to solve, and it establishes the objective function and determines the relevant parameters and solves them. Then, the stitching parameters can be obtained.

2.4. Principle of Particle Swarm Optimization. Ideally, the surface shapes of the two subaperture overlapping areas are identical, but in the actual measurement process, the surface shapes of the two subaperture overlapping areas are not equal due to mechanical motion errors. Assuming that the datum shape of the overlapping area is $\rho_{\text{base}'}$, the surface shape to be spliced with datum is $\rho = f(\rho_0, \theta_0, \alpha, \beta)$, and the difference between the two is the value of the surface shape:

$$\Delta\rho = \rho_{\text{base}} - \rho. \tag{16}$$

In order to reduce the influence of the error, the error of the least square cylinder is used to describe the actual cylinder. The least square cylinder indicates the sum of the squares of the radial distances from the cylinder to the points on the actual cylinder is the minimum, that is,

$$\min \Delta\rho = \sqrt{\sum_{i=1}^{N} \Delta\rho_i^2}. \tag{17}$$

In formula (17), N is the number of points in the overlapping region. When $\Delta\rho$ approaches the minimum value of 0, corresponding $(\rho_0, \theta_0, \alpha.\beta)$ is the solution of the system of equation (16).

Using the particle swarm optimization algorithm, it is necessary to determine some parameters. By consulting the relevant literature, it can be known from [22] that when c_1, c_2 is not 0, it is called a complete particle swarm algorism, and the value is easier to maintain the convergence speed and the balance of the search results, which is a better choice, so this paper sets c_1, c_2 to the random number $[0, 1]$. Shi and Eberhart discussed the influence of inertia weight between $[0, 1.4]$ [23]. The conclusion is that when $\omega \in [0.8, 1.2]$, the convergence speed will be increased, and when $\omega > 1.2$, the convergence will fail. So, ω is chosen as 0.96 in this paper.

The flowchart of the particle swarm algorithm is shown in Figure 6.

Through the analysis of the principle and the whole idea of this paper, the flowchart of the whole frame of this principle is shown in Figure 7. It was verified by using experiments.

3. Experiments

3.1. Composition of the Experimental Device System. Figure 8 shows an optical path diagram for measuring the three-dimensional topography of an object by using a tilt illumination light method, and Figure 9 shows a physical diagram. MO is the microscopic objective, and PH is the pinhole device; MO and PH can be combined as a pinhole filter, which can make the laser light become the ideal point Olite. BS1 and BS2 are beam splitters, M1, M2, and M3 are mirrors, BA is a beam attenuator, L1 and L2 are lenses, L1 has a focal length of 100 mm, and lens L2 has a focal length of 200 mm. Lens L2 is mounted on a high-precision displacement platform PI with a translation accuracy of 20 μm. It can move the illumination light vertically in the direction perpendicular, which makes the angle of illumination light change slightly. The propagation process of the light path is as follows: the laser light emitted by the laser passes through MO, PH, and BE to become uniform parallel light. The parallel light is divided into two paths of light through BE1, one of parallel light passes through BA and mirror M3 as reference light comes into CCD; the other path of the parallel light is reflected by M1 and M2 after focusing and collimating by lens L1 and L2, which passes the displacement platform. Then, the object is illuminated; finally, the CCD receives the scattered light emitted from the surface of the object.

The experiment uses a green light laser with a wavelength of 532 nm. The pixel number of CCD is 2748 (H) × 3664 (V), the single pixel value is 1.67 μm, the pixel size of the whole CCD is 4.6 mm (H) × 6.1 mm (V), the illumination light tilt angle $\theta = 11^\circ$, the recording distance is 290 mm, the moving distance of lens L2 on the translation table is 30 um, and the change of the inclination angle of illumination light is $\Delta\theta = 0.03/200$ rad $\approx 0.0086^\circ$. The relation between the reference light and the object light meets the conditions including the spectral separation condition and the sampling theorem [24] in the off-axis digital hologram. And the intensity ratio of the reference light and the object light meets the optimum intensity ratio, that is, 1 : 1.

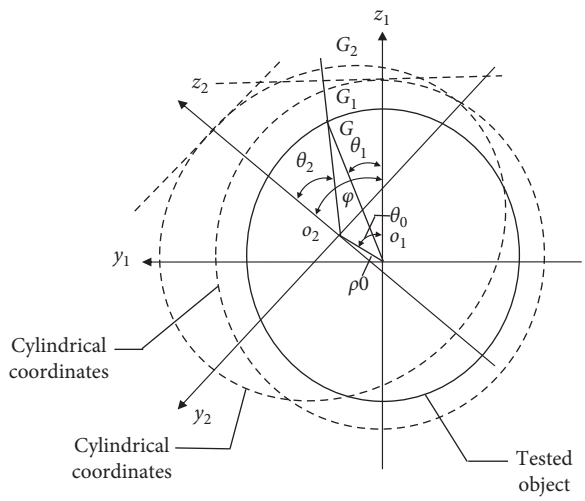

Figure 5: Coordinate transformation relations in cylindrical.

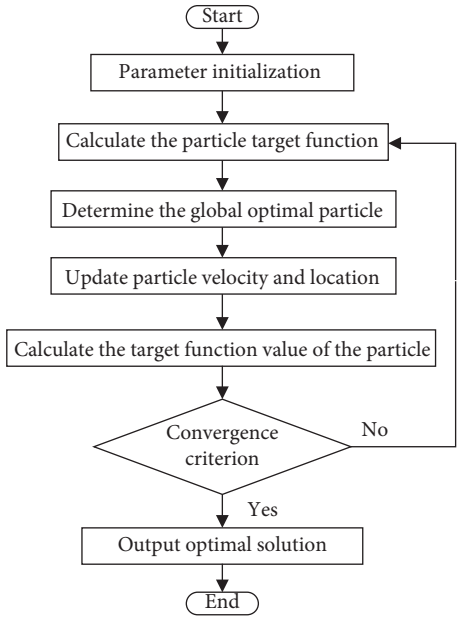

Figure 6: Particle swarm optimization solution flowchart.

3.2. The Effect of Specular Reflection and Diffuse Reflection on Reconstructed Image Quality. In this experiment, the nut and the stud are used. The nut is screwed on the stud and fixed together on the rotary stage. The rotary stage is fixed on the pneumatic platform. Due to the nut of specular reflection and diffuse reflection on the surface, the quality of the reconstructed image will be affected, and the quality of the reconstructed image directly affects the quality of the next interference fringe image, which also affects the influence of the three-dimensional shape measurement. At the same time, the reconstructed image quality is low, and the contrast is poor. Even with the image plane filtering technique, it is not easy to find the image formed by the object on the 1-FFT plane. Figure 10 shows the effect of image reconstruction on the 1-FFT image plane by using the mirror reflection and diffuse reflection of nuts, respectively, and the result of

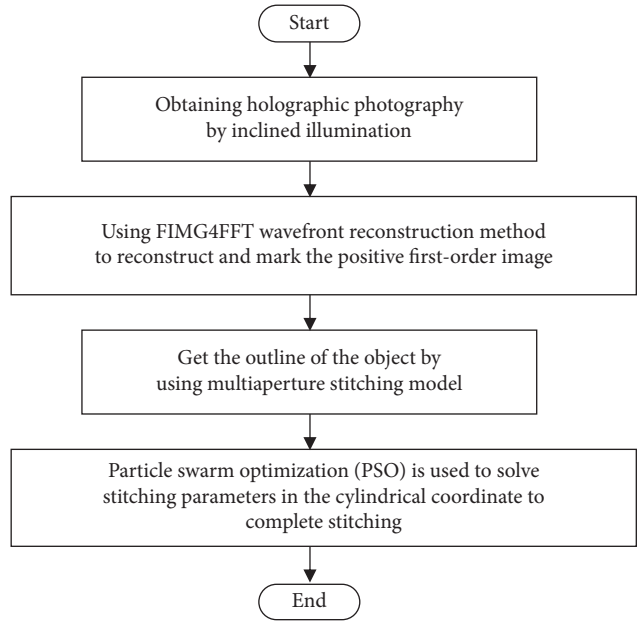

Figure 7: The entire framework flowchart of this principle.

angular spectrum reconstruction will be obtained after image filtering. It can be seen that the image of the diffuse reflection object on the 1-FFT plane is very unclear, so a marking method of the 1-FFT reconstruction image plane is proposed here. In this experiment, it is easy to find the position of the first-order image of the 1-FFT reconstruction plane by using the specular reflection of the nut. Then, the nut is rotated so that the reflected light from the mirror is far away from the CCD and the diffuse reflected light from the nut enters the CCD. Because the nut is fixed on the rotating table, it only rotates, and its spatial position does not change, so the angle of the reference light does not change, so the diffuse reflection image can be obtained at the same position on the 1-FFT reconstruction image plane. Figure 11 shows the flowchart of the 1-FFT reconstructed image plane positive first-order image marking method.

Figure 12 analyses the reconstructed image of specular reflection and diffuse reflection. It can be seen that when the specular reflection is strong, the reconstructed image can only see one side of the nut. When the reflected light of the specular surface is gradually weakening, the reconstructed nut using diffuse reflection has a better effect. The quality of the reconstructed image directly affects the quality of the phase difference image because the fringe produced by the phase difference image is subtracted from the phase of the two reconstructed images, which affects the quality of the phase map.

3.3. Calibration of Height Measurement Error. In order to estimate the height measurement error of the digital holographic tilt illumination method, two measuring blocks are combined to form a ladder-shaped object with a height of 9 mm, that is to say, two parallel planes are used to form an object with a height difference of 9 mm. As it is shown in Figure 13, in order to make the two measuring blocks

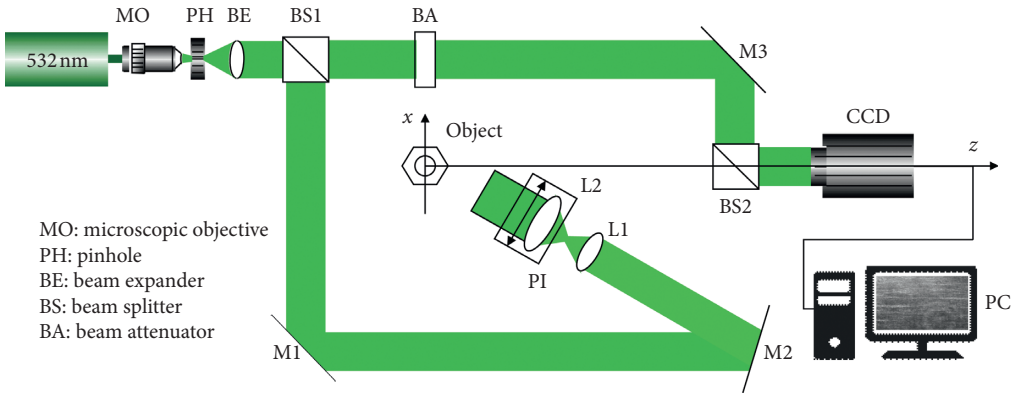

Figure 8: Experimental optical path map of inclined illumination light measurement.

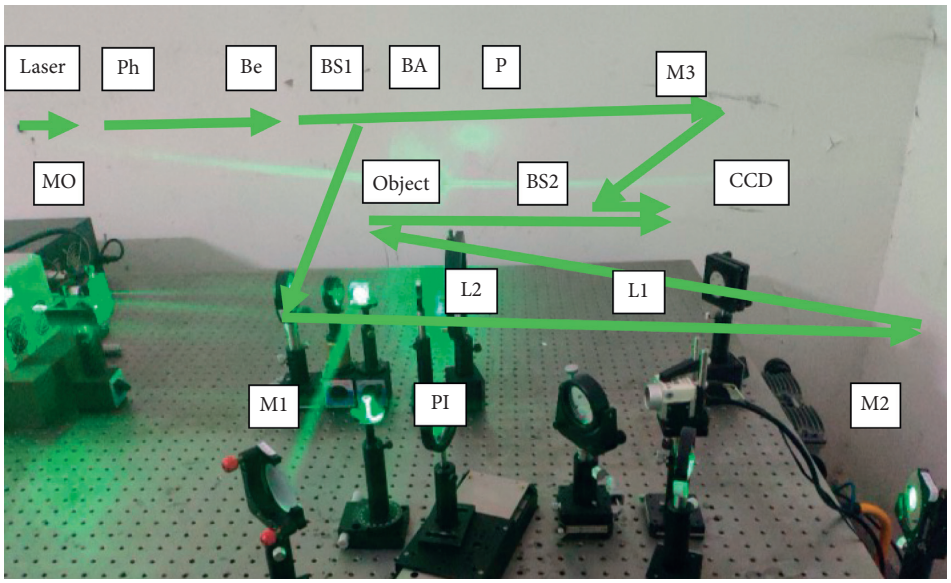

Figure 9: The diagram of the experimental device for measuring inclined illumination light.

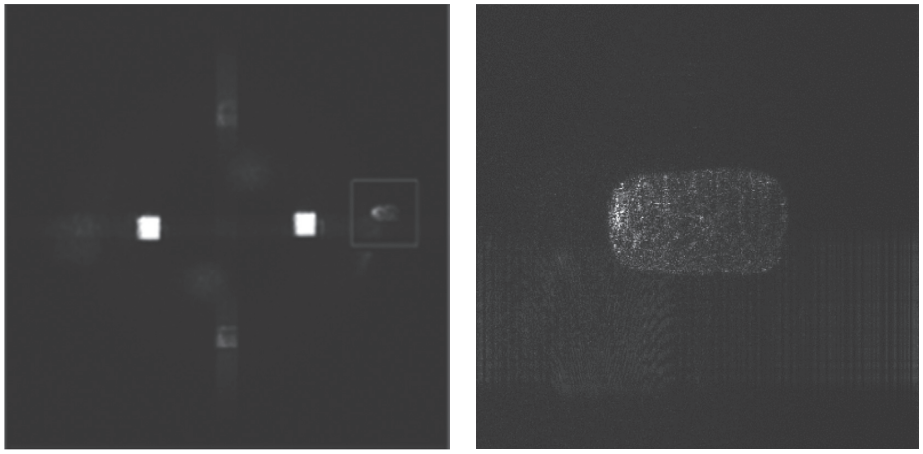

(a) (b)

Figure 10: Continued.

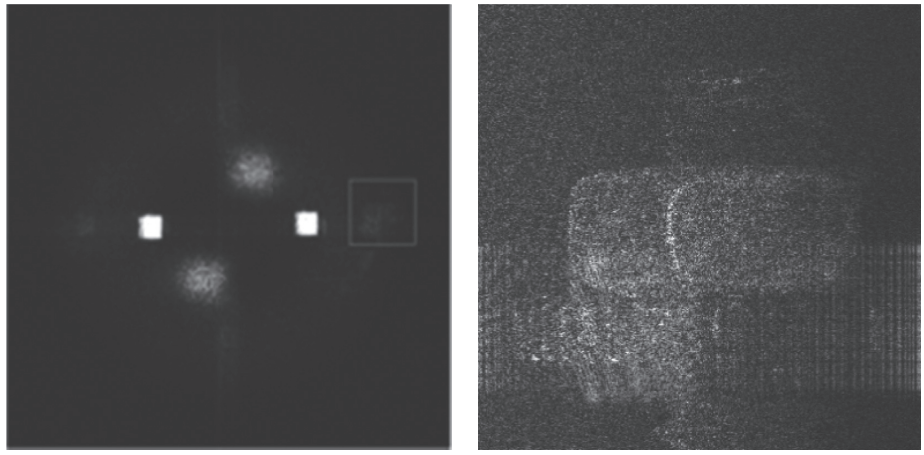

(c) (d)

Figure 10: Reconstruction results of specular and diffuse reflectance. (a) Result of specular reflection on the 1-FFT plane. (b) Reconstruction of the specular reflection image after filtering. (c) Results of diffuse reflection on the 1-FFT surface. (d) Reconstruction of the diffuse reflectance image after filtering.

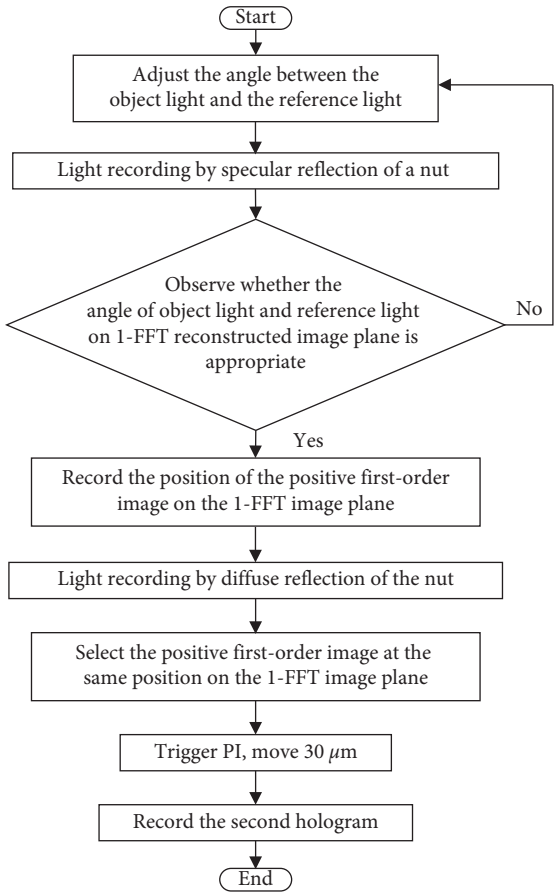

Figure 11: Flowchart of the 1-FFT reconstructed image plane positive first-order image marking method.

together, a magnet is used to absorb the back of one measuring block.

Because these two measuring blocks are standard gauge blocks, tolerance is very small and can be accurate to the submicron level. But, as a standard gauge block, the verification of measurement accuracy is also required. As for a measuring tool, its measurement accuracy must reach submicron level to measure the height difference between gauge block1 and gauge block2. Based on this, we choose an electric vernier caliper with an accuracy of 0.01 mm as the measurement tool. It is shown in Figure 13. Figure 14(a) shows an enlarged view of the reading dial in Figure 14(b). As it can be seen from Figure 14(b), the accuracy of the electric vernier caliper is 0.01 mm, which has reached the submicron level.

The measure method of the electric vernier caliper is as follows.

First, using the electric vernier caliper is to measure the distance of A in Figure 13. The distance of A is a total long distance.

Second, similarly, using the electric vernier caliper is to measure the distance of B in Figure 13. The distance of B is a passive distance.

Third, subtracting B from A is to get the height difference between gauge block1 and gauge block2.

Since the upper and lower surfaces of gauge blocks 1 and 2 are both polished, they can be measured as standard measuring objects. The area marked by the red line in Figure 13 is the measurement data section. The whole height of C will be measured (the height difference between gauge block1 and gauge block2). The measurement data are shown in Table 1. It can be seen from the average value of the measurement data that the error of the standard gauge block is only 0.044%. It can be used as a standard gauge block for calibration.

Then, the inclined illumination light method is used to measure. Firstly, two digital holograms before and after illumination tilt are taken, and then the 1-FFT reconstruction image is obtained by reconstruction, respectively. The interference-free FIMG4FFT reconstruction image is obtained by image plane filtering technology. The phase difference image is obtained by subtracting the phase image before and after illumination tilt. Then, the linear tilt term related to X is removed and then filtered. Figures 15(a)–15(f)

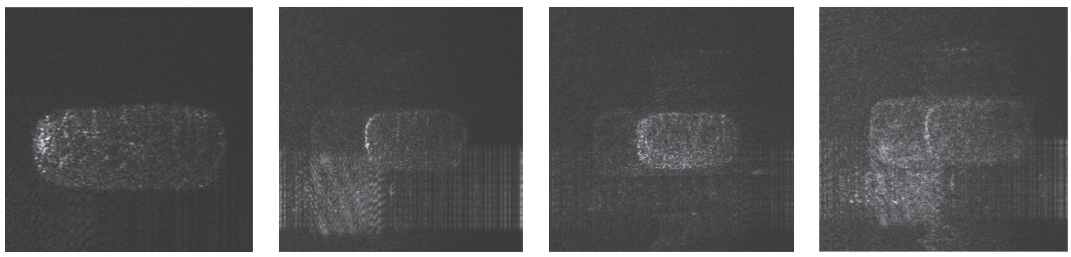

(a) (b) (c) (d)

Figure 12: Specular reflection gradually weakening effect. (a) Strong specular reflection. (b) Specular reflection weakened. (c) Simultaneously exist. (d) Diffuse reflection.

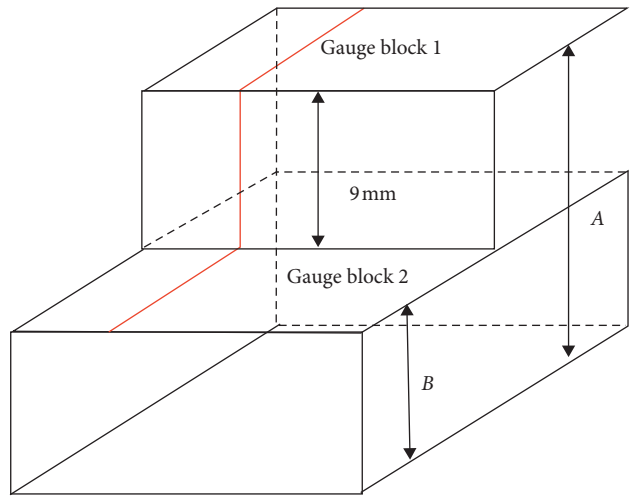

Figure 13: Combine two gauge blocks into one object with a height difference of 9 mm.

(a) (b)

Figure 14: The electric vernier caliper: (a) the physical map; (b) the reading dial.

show one of the holograms, 1-FFT reconstructed image, FIMG4FFT reconstructed image, phase difference image, image after removing the linear tilt term, and image after denoising.

In order to display visually, the height difference portion is taken out for analysis. The contour image corresponding to the red lines in the red rectangular frame and the red rectangular frame in Figure 15(f) is shown in Figures 16 and 17.

As it can be seen from Figure 17, the height difference between the two planes is about 8.891 mm. In order to obtain more accurate experimental results, the phase curves of four positions are randomly selected in the phase image, and the error range of height measurement is from 0.1 mm to 0.5 mm, and the maximum relative error is 5.6%.

3.4. Contour Acquisition and Mosaic of Rotary Three-Dimensional Objects. The threaded part under the nut which is the double-headed stud is measured and spliced in three-dimensional digital holography. The size of the stud is M6. The flowchart of the object contour is shown in Figure 18.

Table 1: The height difference between gauge block1 and gauge block2 (mm).

Category	Time					
	1	2	3	4	5	Average
A	14.00	13.99	14.00	14.01	14.00	14.00
B	5.00	5.01	5.00	5.00	4.99	5.00
C	9.00	8.98	9.00	8.99	9.01	8.996

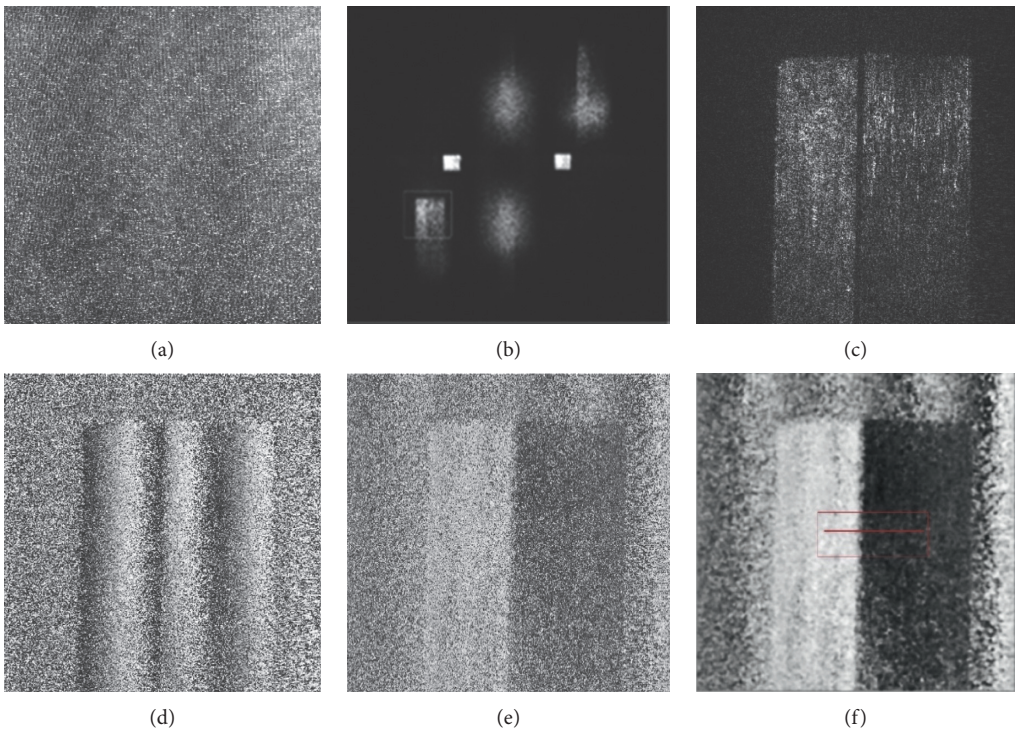

Figure 15: Measuring height of the measuring block by the inclined illumination method: (a) digital hologram; (b) 1-FFT reconstruction image; (c) FIMG4FFT reconstruction image; (d) phase difference image; (e) remove linear tilt terms; (f) image after denoising.

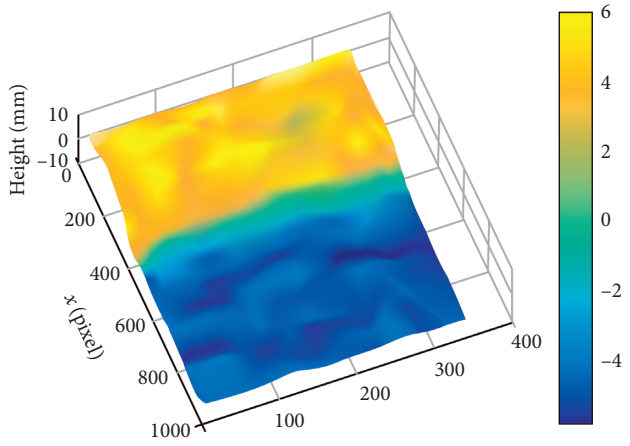

Figure 16: The contour image of the red box in Figure 15(f).

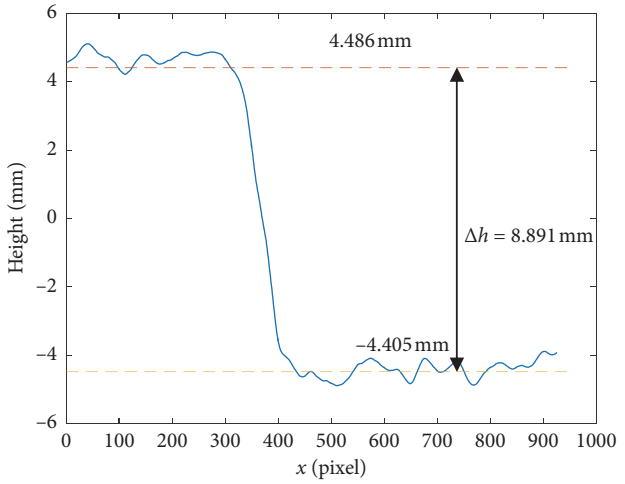

Figure 17: The curve corresponding to the red line in Figure 15(f).

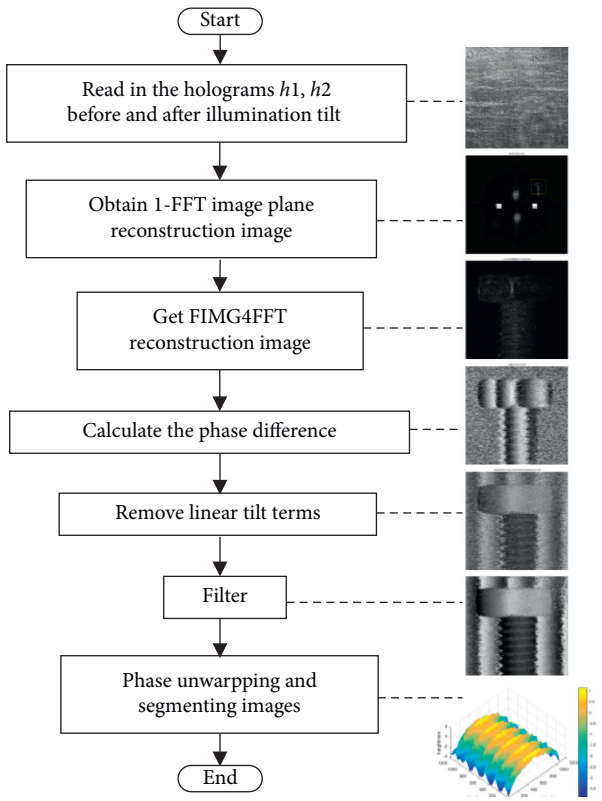

Figure 18: Obtaining an object outline flowchart.

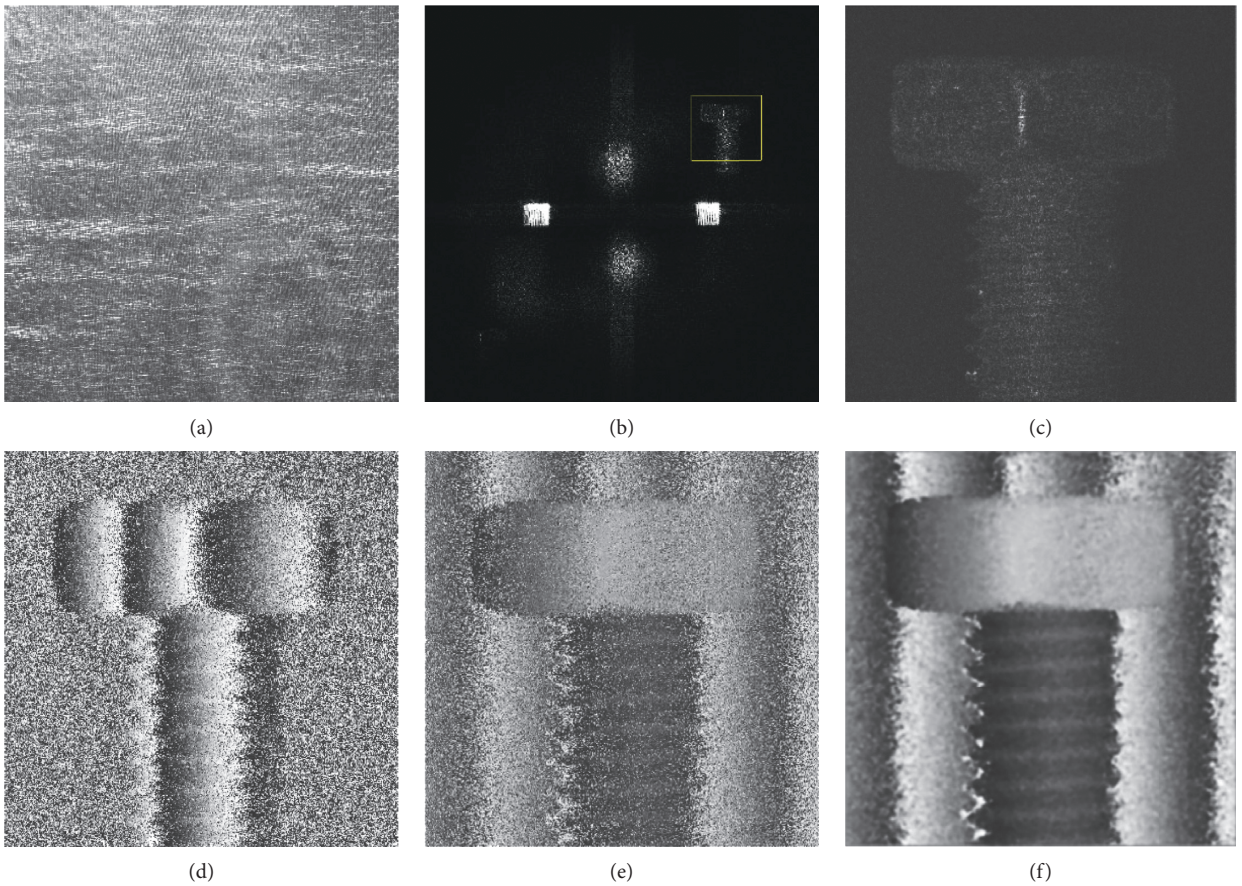

Figure 19: Inclined light illumination measures the contour of a stud. (a) Digital hologram. (b) 1-FFT reconstruction image. (c) FIMG4FFT reconstruction image. (d) Phase difference image. (e) Remove linear tilt terms. (f) Image after denoising.

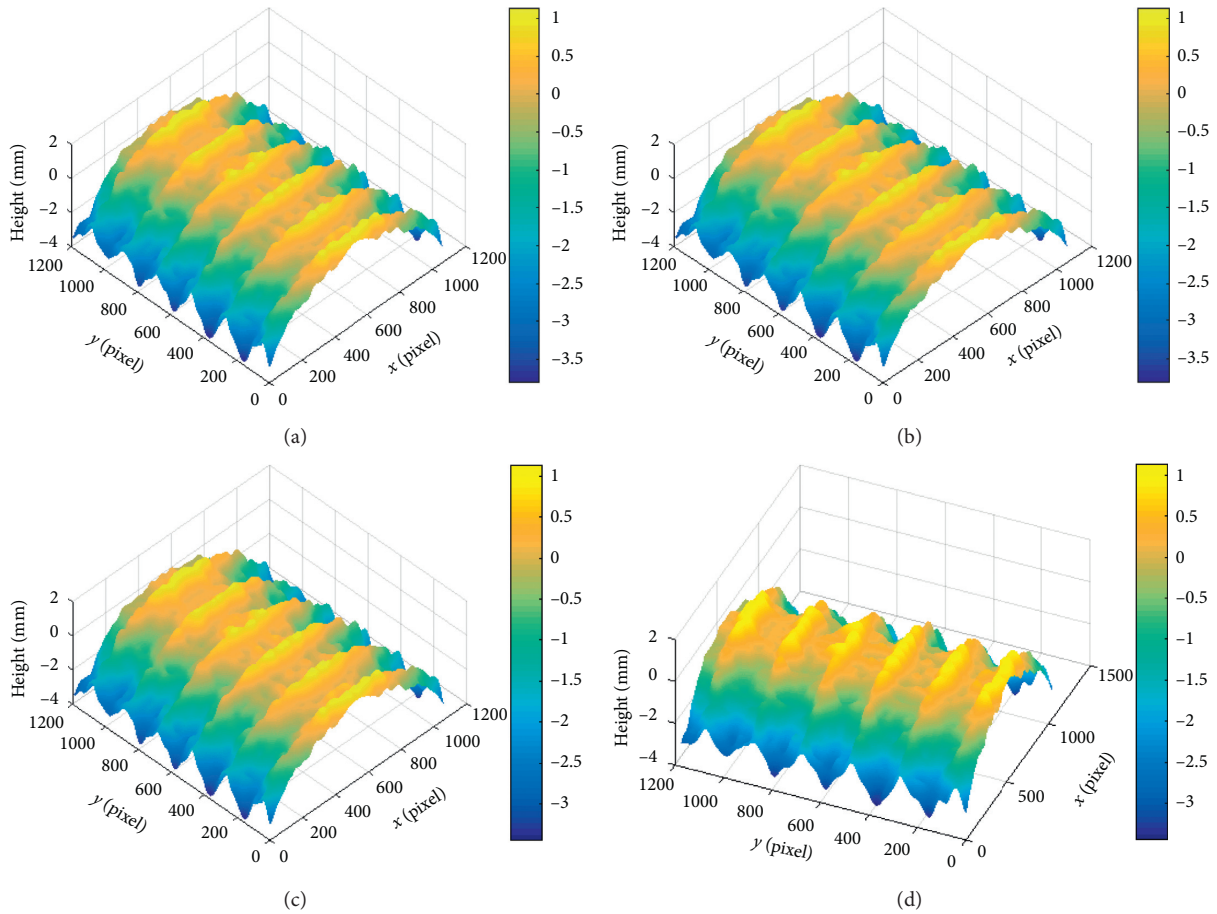

Figure 20: Three-dimensional phase distribution of studs at each viewing angle: (a) 0°; (b) 90°; (c) 180°; (d) 270°.

Because the stud is similar to a cylinder, a single angle of view can capture half of the area of the stud, and the corresponding circumference angle is 180°. The whole stud is recorded four times, which means the image of the first view was taken at a viewing angle of 0°, and then the rotating table is rotated by 90° to obtain an image at the second viewing angle so that the corresponding circumferential angle of the overlapping regions at the two viewing angles is 90°, and the overlap area is 50%. According to the steps of the flowchart, the contour of the double-headed stud is obtained. Figure 19 shows the contour of the double-headed stud measured by the inclined illumination method. Figure 20 shows the phase distribution of the three-dimensional reconstruction of the stud from different perspectives. Figure 21 shows the three-dimensional morphology of the stud after splicing, and it can be seen that the effect is good.

As it is shown in Figure 21, the three-dimensional splicing contour map of the stud has been completed, and the similarity of the stitching is basically consistent with the original object. Although the error analysis between the real object and the stitched object is not done, it can be seen from the visual comparison of the stitched object and the real object that the stitched object is very similar to the real object. Therefore, the stitching theory described in Chapter 2 is correct. This technique is of great significance for 3D reconstruction and stitching of digital holography.

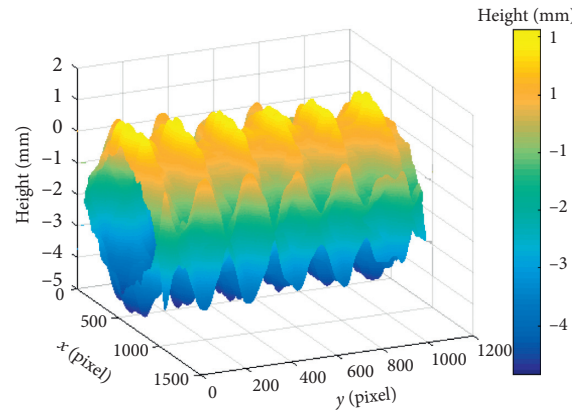

Figure 21: Three-dimensional topography after stud splicing.

4. Conclusions

The reconstruction image of a weak diffusely reflecting object has poor contrast because of its low light intensity and the position of the positive first-order image cannot be located accurately. All of results will influence the quality of subsequent acquisition of the interference phase map. A premarking method is proposed in this study, which combines the FIMG4FFT method and changes the inclination of the illumination light. A calibration target with a

height difference of 9 mm is used in demonstration test. The results show that the measurement error is between 0.1 mm and 0.5 mm, and the maximum relative measurement error is 5.6%. The multiaperture stitching technique in cylindrical coordinates is applied to accomplish the digital holographic 3D stitching. The particle swarm optimization algorithm is used to transform the nonlinear equations into optimization problems to solve the splicing parameters. The contour from a single viewpoint is stitched together to realize the three-dimensional display of the whole object. Finally, the three-dimensional stitching of rotational three-dimensional objects in the cylindrical coordinate system is carried out, and the experiment for a mechanical part has been conducted.

Data Availability

Data are available from Yan Yang (yangyan@cqut.edu.cn).

Conflicts of Interest

The authors declare that they have no conflicts of interest.

Acknowledgments

This work was supported by the National Natural Science Foundation of China (nos. 11272368 and 51875068), the International Cooperation Special Project in Science and Technology of China (no. 2015DFR70480), the Chongqing Municipal Education Commission's Science and Technology Research Project (KJ1600929), and the Graduate Innovation Foundation of Chongqing University of Technology (no. ycx2018216).

References

[1] B. Li, Y. P. Luo, Z. Wang et al., "Research on fast measurement method of 3D contour of multi-light knife," *Acta Photonic a Sinisa*, vol. 32, no. 6, pp. 738–741, 2003.

[2] F. Li and C. L. Zhou, "A new dual-frequency grating profilometry," *Acta Photonic a Sinisa*, vol. 34, no. 4, pp. 632–635, 2005.

[3] P. Sun, L. Zhang, and C. X. Tao, "Measurement of 3D morphology of objects based on fourier transform method of LCD digital projection technology," *Acta Photonic a Sinisa*, vol. 34, no. 8, pp. 1250–1252, 2005.

[4] I. Yamaguchi and T. Zhang, "Phase-shifting digital holography," *Optics Letters*, vol. 22, no. 16, pp. 1268–1270, 1997.

[5] I. Yamaguchi, J.-I. Kato, and S. Ohta, "Surface shape measurement by phase-shifting digital holography," *Optical Review*, vol. 8, no. 2, pp. 85–89, 2001.

[6] G. Pedrina, F. Philipp, J. Hans et al., "Shape measurement of microscopic structures using digital holograms," *Optics Communications*, vol. 164, no. 4–6, pp. 257–268, 1999.

[7] Z. Y. Feng, F. Jia, J. H. Zhou et al., "Three-Dimensional surface shape measurement of big objects by image splicing in digital holography," *Chinese Journal of Lasers*, vol. 35, no. 12, pp. 2017–2021, 2008.

[8] F. Jia, Z. Y. Feng, L. B. Zhou et al., "Pre-imaging digital holography for measuring 3D morphology of large objects," *Acta Photonica Sinica*, vol. 37, no. 11, pp. 2239–2243, 2008.

[9] X. M. Guo, C. Chen, and W. S. Wang, "Three-Dimensional shape test based on digital holography," *Natural Science*, vol. 1, no. 1, pp. 34–38, 2015.

[10] J. C. Li, "Introduction of digital color holographic wavefront reconstruction algorithm," *Chinese Journal of Lasers*, vol. 38, no. 5, Article ID 0501001, 2011.

[11] J. Li and Z. Peng, "Statistic optics discussion on the formula of digital holographic 3D surface profiling measurement," *Measurement*, vol. 43, no. 3, pp. 381–384, 2010.

[12] J. C. Li, "Statistical optical discussion of digital holographic detection process of scattered light," *Acta Photonica Sinica*, vol. 37, no. 4, pp. 734–739, 2008.

[13] J. C. Li, *Diffraction Calculation and Digital Holography*, Science Press, Beijing, China, 2014.

[14] W. G. Joseph, *Introduction to Fourier Optics*, Roberts and Company Publishers, New York, NY, USA, 2005.

[15] P. Picart and J. Leval, "General theoretical formulation of image formation in digital Fresnel holography," *Journal of the Optical Society of America A*, vol. 25, no. 7, pp. 1744–1761, 2008.

[16] J. C. Li, Q. H. Song, J. B. Gui et al., "Research of image plane filtering technique in digital holographic wavefront reconstruction," *Acta Optica Sinica*, vol. 31, no. 9, Article ID 0900135, 2011.

[17] J.-C. Li, Z.-J. Peng, P. Tankam, Q.-H. Song, and P. Picart, "Digital holographic reconstruction of a local object field using an adjustable magnification," *Journal of the Optical Society of America A*, vol. 28, no. 6, pp. 1291–1296, 2011.

[18] J. C. Li, Q. H. Song, P. Pascal et al., "Discussion on off-axis digital holographic wavefront reconstruction algorithm," *Chinese Journal of Lasers*, vol. 41, no. 2, Article ID 0209008, 2014.

[19] H. Y. Wang, *Imaging Theory and Experimental Demonstration of Digital Holographic Microscopy*, Beijing University of Technology, Beijing, China, 2008.

[20] W. M. Cheng, M. Y. Chen, Z. Ding et al., "Measurement of three-dimensional shape by multi-aperture stitching in cylindrical coordinates," *Acta Optica Sinica*, vol. 19, no. 6, pp. 92–96, 1999.

[21] H. W. Guo, *360° Profilometry by Multi-Aperture Overlap-Scanning Technique*, Shanghai University, Shanghai, China, 2001.

[22] F. Bian, *Research and Application of Particle Swarm Optimization Algorithm in TSP*, Jiangnan University, Wuxi, China, 2008.

[23] Y. H. Shi and R. C. Eberhart, "A modified particle swarm optimizer," in *Proceedings of the IEEE World Congress on Computational Intelligence*, Anchorage, AK, USA, May 1998.

[24] H. Wang, D. Wang, J. Xie et al., "Analysis of recording conditions of digital hologram by maximum spatial frequency," *Acta Photonica Sinica*, vol. 36, no. 4, pp. 645–649, 2007.